Experimental Investigation of Nozzle Geometry Effect on the Characteristics and Structure of Submerged Twin Jets

by

Chidiebere Felix Nwaiwu

A Thesis submitted to the Faculty of Graduate Studies of
The University of Manitoba
in partial fulfilment of the requirements of the degree of

MASTER OF SCIENCE

Department of Mechanical Engineering
University of Manitoba
Winnipeg

ABSTRACT

The effects of nozzle geometry on the mean and turbulent characteristics of submerged twin jets were experimentally investigated. The experiments were conducted at fixed Reynolds number and offset height ratio of $4{,}400$ and $h/d = 2$, respectively. The jets were produced from three nozzle geometries: round, square, and rectangle, with the rectangular nozzle geometry oriented in the minor (rect_min) and major (rect_maj) planes. The twin nozzles of each geometry type were aligned parallel to the free surface, and the separation ratio between the twin jets was fixed at $G/d = 2.3$ for all cases. Velocity measurements were obtained using a particle image velocimetry (PIV) technique, and analyses of various quantities such as the instantaneous, mean, and surface velocities, as well as the turbulent statistics were performed. The jet-free surface interaction was examined using mean and turbulent velocities at the free surface, velocity defect, and vorticity thickness. Results from the velocity contours showed that the shear layer expansion was most rapid in twin jets produced from the rect_min nozzle geometry, which resulted in the shortest attachment length to the free surface. The instantaneous velocity field showed the most prograde and retrograde vortices in the rect_min nozzle geometry, accounting for the fastest shear layer expansion. Surface-normal profiles of the Reynolds stress ratio showed an enhancement of about 60% at the free surface. The mean surface velocity revealed that the free surface was in a state of strain due to alternating velocity gradient and was most intense in the rect_min jet. Large-scale structures produced along the centreline of the jet father away from the free surface showed a larger streamwise extent compared to those along the centreline of the jet closer to the free surface and were independent of nozzle geometry. Analysis of the joint probability density function of the streamwise and surface-normal velocity fluctuations showed that within the shear layer, the

Reynolds shear stress producing events were dominated by slow entrainment and fast ejection events, and the damping effect of the free surface was least on the rect_min jets.

ACKNOWLEDGMENT

I would like to express my appreciation to advisors Dr. Mark F. Tachie and Dr. Martin Agelin-Chaab for their guidance throughout this program. This work would not have been possible without their invaluable support in times of despair.

To the members of my research group, I am forever grateful for the time made available to me to ensure that this work is a success. Most especially, I would like to appreciate Dr. Mohammad Shajid Rahman, Dr. Baafour Nyantekyi-Kwakye and Ramin Naseri Oskouie for their willingness to answer whenever I called.

I am grateful to the University of Manitoba, Faculty of Graduate Studies, Faculty of Engineering and Department of Mechanical Engineering for the financial support granted to me in the form of scholarships and awards. To Natural Science and Engineering Research Council of Canada (NSERC), I say thank you for the funding made available to conduct this research.

To my wife, siblings, and parents, words fail me to express my deep-rooted appreciation. The love and support from all of you cannot be quantified. In this life and that to come, I will still those you all.

DEDICATION

This thesis is dedicated to my wife – Juliet and my Mother – Cordelia for seeing that which I could not see in me. Your prayers and love have sustained me.

TABLE OF CONTENT

LIST OF FIGURES

LIST OF TABLES

NOMENCLATURE

English Symbols

A_p	Attachment point
a_1	Townsend structure parameter
C	Correlation matrix
C_p	Combined point
C_μ	Modelling coefficient
d	Nozzle diameter (mm)
d_p	Particle diameter
d_{pitch}	Pixel pitch
E	Total energy
E_λ	Fractional energy
F_r	Froude number based on exit velocity and offset height from the free surface
G	Surface-normal separation distance between the twin jets
g	Acceleration due to gravity
h	Surface-normal distance from the centerline of nozzle A to the free surface
H	Surface-normal distance from the centerline of nozzle B to the bottom wall of the channel

K_d	Velocity decay rate
K_s	Spread rate
$K_{d,f}$	Velocity decay rate in the far-field of a free jet
L	Nozzle length
L_a	Attachment length
L_{cp}	Combined point distance
L_{mp}	Merging point distance
L_{uu}^{x}	The streamwise extent of the streamwise two-point velocity autocorrelations
L_{vv}^{y}	The surface-normal extent of the surface-normal two-point velocity autocorrelations
M_f	Magnification factor
M_p	Merging point
N	Number of snapshots
$Q1, Q2, Q3, Q4$	Four quadrant events of the Reynolds shear stress
R_e	Reynolds number based on jet exit velocity and nozzle diameter
R_{uu}	Two-point velocity autocorrelations of the streamwise velocity fluctuations
R_{vv}	Two-point velocity autocorrelations of the surface-normal velocity fluctuations

k	Turbulent kinetic energy
U_j	Jet exit velocity
U_m	Local maximum mean velocity
U_{max}	The local maximum mean velocity of flow
U_s	Surface mean velocity
U, V, W	Streamwise, surface-normal and spanwise mean velocities, respectively
u, v, w	Streamwise, surface-normal and spanwise velocity fluctuations, respectively
$\langle u^2 \rangle$	Streamwise Reynolds normal stress
$\sqrt{\langle u^2 \rangle}$	Streamwise turbulence intensity
$-\langle uv \rangle$	Reynolds shear stress
$\langle v^2 \rangle$	Surface-normal Reynolds normal stress
$\sqrt{\langle v^2 \rangle}$	Surface-normal turbulence intensity
V_s	Particle settling velocity
W	Nozzle width
$\langle w^2 \rangle$	Spanwise Reynolds normal stress
x, y, z	Streamwise, surface-normal and spanwise coordinates, respectively
x_g	Geometric virtual origin

x_k	Kinematic virtual origin
y_m	Surface-normal location of local maximum velocity

Subscripts

A	Variable associated with jet A
B	Variable associated with jet B
ref	Reference location
s	Variable associated with the free surface
z	Variable associated with spanwise rotation

Greek Symbol

τ_r	Particle response time
Δt	Time delay between laser pulses
ΔU	Surface mean velocity defect
Δx	Local displacement vector of a particle
λ_{ci}	Imaginary eigenvalue, swirling strength
$\lambda_{ci,z}$	Unsigned swirling strength associated with spanwise vortex core
$\Lambda_{ci,z}$	Signed swirling strength associated with spanwise vortex core
μ_z	Dynamic viscosity of the fluid
υ	Kinematic viscosity

ρ_f	Fluid density
ρ_p	Particle density
ω_z	Spanwise fluctuating vorticity
$y_{0.5}$	Jet's half velocity width
σ	Spread parameter

Mathematical Symbol

$\langle\cdot\rangle$	Ensemble average

Acronym

AR	Aspect ratio
CCD	Charge-coupled device
FFT	Fast Fourier transform
FOV	Field of view
IA	Interrogation area
JPDF	Joint probability density function
LDV	Laser Doppler velocimetry
Nd:YAG	Neodymium: Yttrium Aluminum Garnet
PIV	Particle image velocimetry
POD	Proper orthogonal decomposition

TKE	Turbulent kinetic energy
2C	Two-component
2D	two-dimension
3C	three-dimension

CHAPTER 1

INTRODUCTION

There is considerable interest in the study of turbulent free-shear flows, including jets, wakes, and mixing layers in engineering because of their enhanced mixing and momentum transfer characteristics. Of particular interest to hydraulic engineers are submerged turbulent jets issuing in the proximity of a free surface. In these cases, the jets are offset from the free surface and upon discharge are deflected towards the surface. This configuration is called a submerged or surface attaching jet. Submerged jets have diverse practical applications, including the remote detection of surface ships, industrial discharge of effluent into shallow rivers, and the release of water from hydro-electric power dams. Despite their numerous applications, however, submerged jets are difficult to predict numerically due to the kinematic boundary condition imposed by the free surface (Rahman et al. 2019). In addition, due to jet confinement, the turbulence dynamics in submerged jets are relatively more complex when compared to the prototypical free jet. The simplest configuration of multiple submerged jets is the twin-submerged jets issuing from two identical parallel nozzles. Thus, this study aims to investigate the mixing and turbulent characteristics of submerged twin jets and to elucidate the dynamics of the coherent structures.

In comparison to submerged jets, considerable studies on turbulent free jets abound. The absence of boundaries or restrictions in turbulent free jet results in less complicated dynamics compared to submerged surface attaching jets. Studies on turbulent free jets include investigations on a single free jet (Abdel-Rahman et al., 1996; Aleyasin et al., 2017a; 2017b; Deo et al., 2007; Ghasemi et al., 2015; Mi et al., 2013; Namer and Ötügen, 1988) and twin free jets (Aleyasin and Tachie, 2019; Harima et al., 2005; Lin and Sheu, 1990; Miller and Comings, 1960; Tanaka, 1970, 1974).

Evidence from these studies suggests better mixing capabilities of twin free jets over single free jets. There have been investigations on the effect of nozzle types such as smooth contraction nozzles, orifice plates (or sharp-edged) nozzles and pipe nozzles in turbulent free jet (Mi et al., 2001; Antonia and Zhao, 2001; Xu and Antonia, 2002; Quinn, 2006). Of the three nozzle types, the smooth contraction nozzle possessed intermediate mixing characteristics. Appreciable investigations have concentrated on understanding the effect of nozzle geometries such as circular and non-circular nozzles (Ricou and Spalding, 1961; Wygnanski and Fiedler, 1969; Abdel-Rahman et al., 1996; Fellouah et al., 2009; Ball et al., 2012; Mi et al., 2013). Studies on free jets issuing from non-circular nozzles include (Hashiehbaf and Romano, 2013; Ho and Gutmark, 1987; Hussain and Husain, 1989; Lee and Baek, 1994; Mi and Nathan, 2010; Quinn, 1992; Schadow et al., 1988). Notable conclusions suggest that jets produced from non-circular nozzle geometries exhibit superior mixing performance, and this is linked to the axis-switching phenomenon due to the self-induction of the asymmetric coherent structures.

Robinson, (1991) defined coherent structure with respect to coherent motions within a three-dimensional flow field where a flow variable correlates significantly with itself or another variable over a range of space and/or time that is significantly larger than the smallest local scales of the flow. These structures occur due to the instability of shear layers as described by the Kelvin-Helmholtz instability theory (White and Nepf, 2007). The nature and existence of these structures are not universal as different boundary conditions alter the structural dynamics. These structures are responsible for the transport of mass, momentum, and heat (Hussain, 1983) and also influence the mixing characteristics of a jet.

There have been considerable investigations into the turbulent free jet, and relatively fewer studies on submerged jets. Despite the enhanced mixing capability of twin jets (Lin & Sheu, 1990) and the fundamental insight into a turbulent flow that stands to be achieved in submerged twin jets study, only a handful of research has been dedicated to it. Figure 1.1 shows a schematic of submerged twin jets, and its salient features, as well as the nomenclature, adopted. The twin jets (Jet A and Jet B) are produced from two parallel nozzles, of diameter, d, with exit velocities, U_j, that issues into a quiescent body of water beneath a free surface. The streamwise and surface normal coordinates are denoted by x and y, respectively, with $x = 0$ and $y = 0$ at the centre of the nozzle in the jet exit plane as shown. U, V, u and v refer to the streamwise mean velocity, surface-normal mean velocity, streamwise fluctuating velocity, and surface-normal fluctuating velocity, respectively. Meanwhile, z, W, w (not shown), represent the spanwise direction, spanwise mean velocity, and spanwise fluctuating velocity, respectively.

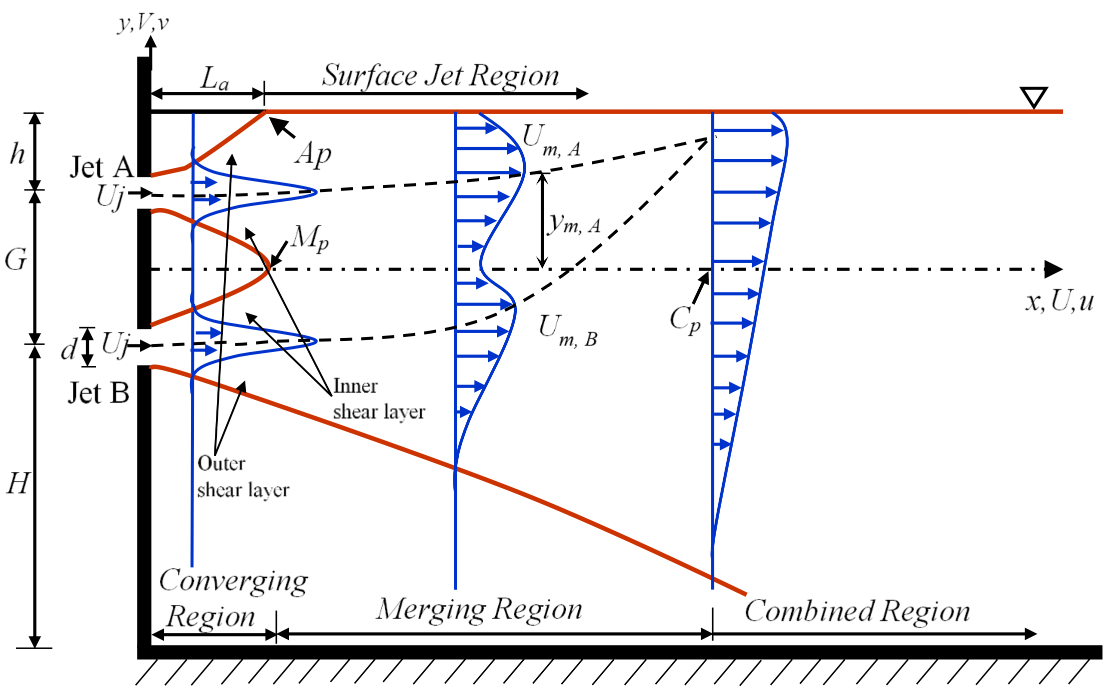

Figure 1.1 A schematic of submerged twin jets interacting with a free surface

The nozzle centrelines of Jets A and B are located at offset heights, h, and H from the free surface and wall, respectively. The nozzle centers are separated by a transverse distance, G. The discharged jets entrain the ambient fluid, resulting in the jet spread and downstream decay of the jet velocity. Due to the restriction imposed by the free surface, a lower pressure region is created between the free surface and the discharged Jet A. This results in the deflection of the outer shear layer of Jet A towards the free surface and the subsequent attachment onto the free surface at the attachment point (A_p). This phenomenon is known as the Coanda effect. Similarly, as shown by Lin and Sheu (1990), a lower pressure region exists between Jets A and B due to the mutual entrainment of the ambient fluid between them. This also results in the deflection of the inner shear layers of both jets and their subsequent convergence at a merging point (M_p). As the jets evolve downstream, they interact with each other and combine to form a single jet at the combined point (C_p). The flow field of submerged twin jet can be sub-divided into three regions as shown. The streamwise distance from the nozzle exit to the merging point is referred to as the converging region. The merging region extends from the merging point to the combined point. Beyond this point is the combined region.

The streamwise distance from the nozzle exit to the attachment point is referred to as the attachment length, L_a. With respect to the free surface, the flow field is categorized into two regions: the pre-attachment region (which corresponds to the streamwise distance from the jet exit plane to A_p), and surface jet region (downstream of A_p). The surface jet region is characterized by non-zero streamwise mean velocity, U_s, at the free surface. The jet-free-surface interaction deflects the location of the local maximum streamwise mean velocity, U_m, from the nozzle centreline towards the free surface (Madnia and Bernal, 1994). The trace of the loci of U_m separates the flow into two shear layers (outer and inner) for each jet as shown by the dashed lines. These dashed lines are referred to as the jet centrelines, while y_m refers to the surface-normal location of U_m with reference to the symmetry plane between the nozzles. $U_{m,A}$ and $U_{m,B}$ refer to the local maximum velocity of Jet A and Jet B, respectively, while $y_{m,A}$ refers to the surface-normal location of $U_{m,A}$.

1.1 Mixing Characteristics

Of great interest in jet application is its mixing efficiency. With respect to twin jets, there is the mixing of the jets with the quiescent ambient as they exit the nozzles and further downstream, to form a single jet. As the jets exit the nozzle, the ambient fluid is entrained into the jet and subsequently results in the decay of the local maximum streamwise mean velocity, U_m and the spread of the jet. The mixing performance of the jets is characterized by the decay and spread rates. In the far-field (region of the flow field where the jet becomes self-similar), the maximum streamwise mean velocity U_m decays linearly with streamwise distance as shown in equation (1.1) (Madnia and Bernal, 1994)

$$\frac{U_j}{U_m} = K_d \left(\frac{x}{d} - \frac{x_k}{d}\right) \tag{1.1}$$

where K_d is the slope of the linear section, otherwise known as the jet decay rate and x_k is the kinematic virtual origin of the jet which is the intercept on the x/d axis.

In a free jet and submerged jet study, Madnia and Bernal (1994) proposed a model based on dimensional reasoning and similarity analysis where the free surface was considered a plane of symmetry. The proposed model described the scaling in the far-field of a surface jet. Their result showed that the maximum streamwise mean velocity followed the straight line shown in equation (1.2) when the velocity profile and streamwise distance are normalized with the offset height ratio, h/d.

$$\frac{U_j d}{U_m h} = \frac{K_{d,f}}{\sqrt{2}}\left(\frac{x}{h} - \frac{x_k}{h}\right) \tag{1.2}$$

$K_{d,f}$ is the far-field decay rate of the corresponding free jet and $\sqrt{2}$ accounts for the momentum of the imaginary jet above the free surface.

The spread of the jet is quantified by the half-velocity width, $y_{0.5}$ that is a measure of the distance from the jet centreline to the transverse or spanwise direction where the local maximum velocity is 50%. In the far-field, $y_{0.5}$ increases linearly with streamwise distance as shown in equation (1.3) (Madnia and Bernal, 1994):

$$\frac{y_{0.5}}{d} = k_s\left(\frac{x}{d} - \frac{x_g}{d}\right) \tag{1.3}$$

where k_s is the spread rate and x_g is the geometric virtual origin.

From literature, a number of parameters that influence the dynamics of submerged jets have been identified. They include Reynolds number, $Re = U_j d/\upsilon$, where υ is the kinematic viscosity (Walker et al, 1995; Wen et al., 2014; Rahman and Tachie 2018), nozzle exit geometry (Tay et al., 2017a) and offset height ratio (Tay et al., 2017b; Essel and Tachie, 2017; Rahman et al., 2018; Essel and Tachie, 2018).

To investigate the influence of the above parameters on the dynamics of submerged jets, different experimental methodologies were adopted over the years. Some of these methodologies include hot-wire (or film) anemometer (Madnia and Bernal, 1994; Swean et al., 1989), Prandtl tube (Raiford and Khan, 2009), laser-Doppler velocimetry (Walker et al., 1995; Sankar et al., 2008), Pitot-static tubes (Rajaratnam and Humphries, 1984; Ead and Rajaratnam, 2001) and particle image velocimetry (Essel and Tachie, 2018; Essel and Tachie, 2016; Rahman et al., 2018; Tay et al., 2017a). With the exception of PIV, the above-listed methodologies are based on pointwise measurement techniques and as such, the result of the studies where they are employed are predominantly limited to one-point statistics. The PIV is a multipoint technique capable of providing whole-field, non-intrusive and simultaneous velocity measurements. It can measure the free surface statistics and instantaneous velocity vectors from whence the visualization and investigation of coherent structures are possible.

1.2 Research Motivation and Objective

While free jet studies suggest better mixing capability of twin jets over a single jet, to the best of the author's knowledge, only (Essel and Tachie, 2017; Essel and Tachie, 2018; Rahman and Tachie, 2018) have investigated submerged twin jets. Their studies focused on offset height and Reynolds number effects. Consequently, the objective of this study is to investigate the effect of nozzle geometry on twin jets dynamics in the vicinity of a free surface. Using multi-point statistics such as two-point correlation and joint probability density function (JPDF), the effect of nozzle geometry on the twin jets interaction will be explored. In addition, the effect of the free surface confinement on the dynamics of the coherent structures will be elucidated.

1.3 Organization of Thesis

Subsequent parts of this thesis are organized as follows: In Chapter 2, detailed review of the literature on two and three-dimensional twin jet, as well as previous investigations on submerged twin jets are presented. Furthermore, techniques for educing coherent structures used in this study are discussed. The experimental setup consisting of the PIV system and the measurement procedure, as well as the experimental test conditions investigated in this study are presented in

Chapter 3. Results and discussions of the experiments are presented in Chapter 4. Finally, in Chapter 5, major conclusions are highlighted along with the recommendations for future study.

CHAPTER TWO

LITERATURE REVIEW

In this chapter, previous studies on free and surface attaching jets are reviewed. Of particular relevance to this study are the investigations on single and twin jets, their dependence on initial conditions, and the dynamics of the coherent structures in turbulent jets. Some of the existing techniques for educing coherent structures are also reviewed.

2.1 Coherent Structures in Turbulent jets

Aside from the definition provided by Robinson (1991), coherent structures are also defined as connected, large-scale turbulent fluid mass with phase-correlated vorticity over its spatial extent" (Hussain, 1983). It should be noted that coherent structures as used herein, refer to the large-scale structures and not the small scales. Understanding the dynamics of these structures will undoubtedly give a greater insight into the mechanism associated with mass and momentum transport in turbulent jets. It is widely accepted that vortical structures in turbulent shear flow consist of different length and time scales identified as integral scales, Taylor microscales, and Kolmogorov scales. The integral length scales, constrained by the flow geometry, is a measure of the size of the largest structures. Taylor microscale is responsible for the transfer of energy from the integral scales to the Kolmogorov scales while the Kolmogorov scales are the scales at which kinetic energy is dissipated due to the significant effect of viscosity.

2.2 Techniques for Educing Coherent Structures

In this section, the applicable techniques used in the present study to educe coherent structures are discussed. These techniques include the two-point correlation, joint probability density function (JPDF), and swirling strength.

2.2.1 Two-point correlation

To investigate the large-scale structures, a two-point correlation of the velocity fluctuations is employed. The two-point correlation function can be used to investigate the spatial coherence of the structures and to estimate the integral length scales. The two-point cross-correlation function (R_{AB}) between two arbitrary quantities $A(x, y)$ and $B(x, y)$ is evaluated following (Volino et al, 2007):

$$R_{AB}\left(x_{ref} + \Delta x, y_{ref} + \Delta y\right) = \frac{\overline{A\left(x_{ref}, y_{ref}\right) B\left(x_{ref} + \Delta x, y_{ref} + \Delta y\right)}}{\sigma_A\left(x_{ref}, y_{ref}\right) \sigma_B\left(x_{ref} + \Delta x, y_{ref} + \Delta y\right)} \quad (2.1)$$

where $\left(x_{ref}, y_{ref}\right)$ denote the reference locations, Δx and Δy denote the spatial separation between *A* and *B* in the streamwise and surface-normal directions, respectively, and σ_A and σ_B are the root mean squares of *A* and *B* at their reference locations, $\left(x_{ref}, y_{ref}\right)$ and spatial separations, $\left(x_{ref} + \Delta x, y_{ref} + \Delta y\right)$, respectively.

2.2.2 Joint probability density function (JPDF)

To investigate the turbulent coherent events that contribute to the production of Reynolds shear stresses, JPDF of the velocity fluctuations, $P(u, v)$ has been adopted following (Tay et al., 2017b; Wallace & Brodkey, 1977) and defined as:

$$\langle uv \rangle = \iint_{-\infty}^{\infty} uv\, P(u, v) du dv \quad (2.2)$$

The velocity fluctuations were sorted into bins and the result interpreted following quadrant analysis where the dominant events were divided into the four quadrants based on shear layer orientation. The quadrants are labelled Q1, Q2, Q3, and Q4. In the upper shear layer of each jet, where $\frac{\partial U}{\partial y} < 0$, Q1 $(+u, -v)$ denotes fast entrainment of ambient fluid; Q2 $(-u, -v)$ denotes slow entrainment of ambient fluid; Q3 $(-u, +v)$ denotes slow ejection of ambient fluid and Q4 $(+u, +v)$ denotes fast ejection of ambient fluid.

2.2.3 Swirling strength

Swirling strength has been used in literature to identify vortical structures within a flow field and to study the induced rotational motion. In the absence of the local velocity gradient tensor in three dimensions as is the case in a planar PIV, a two-dimensional swirling strength can be calculated using the in-plane velocity gradients (Adrian et al., 2000; Hutchins et al.,2005). Following Tay (2015), it is formulated in the vertical jet symmetry plane ($x - y$ plane) as

$$\begin{vmatrix} \frac{\partial U}{\partial x} - \lambda & \frac{\partial U}{\partial y} \\ \frac{\partial V}{\partial x} & \frac{\partial V}{\partial y} - \lambda \end{vmatrix} = 0 \tag{2.3}$$

The solution to equation (2.3) is given by

$$\lambda = \frac{1}{2}\left(\frac{\partial U}{\partial x} + \frac{\partial V}{\partial y}\right) \pm \frac{1}{2}\sqrt{\underbrace{\left(\frac{\partial U}{\partial x} + \frac{\partial V}{\partial y}\right)^2}_{b^2} - \underbrace{4\left(\frac{\partial U}{\partial x}\frac{\partial V}{\partial y} - \frac{\partial V}{\partial x}\frac{\partial U}{\partial y}\right)}_{4ac}} \tag{2.4}$$

Defining the swirling strength λ_{ci} at the location where the solution is complex, its magnitude $\lambda_{ci,z}$, associated with the spanwise vortex core at that location is given as

$$\lambda_{ci,z} = \frac{1}{2}\sqrt{|b^2 - 4ac|} \tag{2.5}$$

where $4ac > b^2$ or otherwise, zero. From equation (2.5), $\lambda_{ci,z} \geq 0$, implying that the swirling strength will be devoid of rotational direction. Hence, to identify positive and negative swirling strength, the sign of the in-plane instantaneous fluctuating vorticity multiplies the swirling strength, $\lambda_{ci,z}$. Thus, the signed swirling strength is given by:

$$\Lambda_{ci,z} = \lambda_{ci,z} \left({}^{\omega_z}/_{|\omega_z|} \right) \tag{2.6}$$

where $\Lambda_{ci,z}$ is the signed swirling strength and ω_z is the fluctuating vorticity.

2.3 Previous Investigations of Coherent Structures in Turbulent Jets

The dynamics of coherent structures have been extensively studied in free jets (Adrian et al., 2000; Agrawal and Prasad, 2002; Aleyasin et al., 2017a; Grinstein et al., 1995; Hussain and Husain, 1989; Liepmann and Gharib, 1992; Mi and Nathan, 2010). The vortex rings formed due to the shear layer instability, pair up and subsequently break up as the jet develops downstream. In this process, the ambient fluid is entrained (Agrawal and Prasad, 2002). Agrawal and Prasad (2002) reported that the average vorticity, circulation, and energy of these vortices depend strongly on Reynolds number. This was in agreement with an earlier study by Liepmann and Gharib (1992) on the effect of Reynolds number on streamwise vortices and entrainment which reported the growth of identifiable vortical structures with increasing Reynolds number. The dependence of a jet's mixing performance on initial conditions such as nozzle type was investigated by Mi et al (2001). They reported that jets formed from a pipe nozzle contained small-scale turbulent structures in the near field which delayed the roll-up and pairing process of these vortices compared to a smooth contraction nozzle. The occurrence of the pairing process results in the entrainment of the quiescent ambient fluid. The impact of a jet's nozzle geometry on mixing was reported by Grinstein et al. (1995). Enhanced mixing was attributed to the axis-switching phenomenon in jets produced from non-circular nozzles. The axis-switching phenomenon is a consequence of self-induced deformation of the vortical structures (due to the presence of corners in non-circular geometries), resulting in axis rotation of the jet cross-section. Aleyasin et al., (2017a) investigated the dynamics of coherent structures in free jets produced from eight different nozzle geometries and a sharp-linear contoured nozzle type. To investigate the effect of nozzle type, the results were compared to jets produced from orifice plate and smooth contraction nozzle (Mi and Nathan 2010). They concluded that the coherent structure size, evaluated by the integral length scale on a jet's centreline, increased linearly with streamwise distance, and were nearly independent of both the nozzle geometries and nozzle types.

In the relatively fewer submerged surface attaching jet studies, the dynamic role of coherent structures are documented by Shinneeb et al. (2011); Wen et al. (2014a); Wen et al. (2014b); Tay et al. (2017a); Tay et al. (2017b); Rahman et al. (2018); Essel and Tachie (2018). The characteristics of large vortical structures were investigated by Shinneeb et al. (2011) at offset heights of 5*d*, 10*d,* and 15*d,* with *d* representing the jet exit diameter. Velocity measurements were obtained in both the vertical and horizontal planes. Their proper orthogonal decomposition (POD) results showed that the size and number of identified vortical structures to vary linearly and inversely, respectively, with increasing streamwise distance. It was observed that free surface confinement restricts the size of the vortices and their circulation in the vertical direction. The effects of the offset height were further explored by Wen et al. (2014b) on the spatial structures using laser-induced fluorescence and time-resolved PIV techniques. Three offset heights of h/d= 2, 4 and 6 were investigated, and the free surface confinement effect decreased with increasing offset height. Specifically, the POD results at h/d = 2 (where the free surface effect was most evident), showed the jet-free surface interaction resulted in an unsteady up-and-down motion of the free surface that produced a surface-normal compression of the subsurface jet flow. Consequently, a downstream oscillation of the free surface was observed. This downstream oscillation was more evident as the offset height ratio increased to h/d= 4. The confinement by the free surface resulted in stretching of the vortical structures and a pairing process was observed similar to the study of Shinneeb et al. (2011). At a fixed offset height of h/d = 2, Wen et al (2014a) examined the effect of Reynolds number (Re=1920 and 3480) on the spatial structures. Using the space-time proper orthogonal decomposition technique, a flapping motion of the jet at Re = 1920 was observed, and the free surface stretched the identified vortical structures. The low Reynolds number jet consisted of larger scales of the dominant structures, while small scale structures were observed in the high Reynolds number jet. The authors attributed the observed small scales in the high R_e jet to the higher momentum flow and strong jet-free surface interaction.

To date, the only investigation of the effect of aspect ratio (AR) on submerged jets was reported by Tay et al. (2017a). They investigated the effect of free surface on the coherent structure in jets produced from rectangular nozzles with aspect ratios of 1, 2 and 4, using two-point velocity and velocity-swirling strength correlations. The results showed prograde and retrograde vortices, and confinement effects led to an enhancement of the sizes of the structures in the streamwise direction and their suppression in the surface-normal direction. Structures in the upper shear layer of the flow showed an increased inclination angle towards the free surface when compared to those in the lower shear layer. The effect of offset height ratio ($h/d = 1,\ 2,\ 3$ and 4) was reported by (Tay et al, 2017b). It was shown that the confinement effect increases with a decreasing offset height ratio. Far downstream and at h/d= 1, turbulent structures identified by the two-point autocorrelation function of the streamwise velocity fluctuation attached to the free surface at an inclination angle similar to what has been previously reported in a wall jet and turbulent boundary layers. As the free surface is approached in the upper shear layer, the streamwise two-point correlation function was enhanced while the surface normal counterpart was suppressed. Generally, the structures were shown to grow as the jet evolved downstream and with an increasing offset height ratio. Rahman et al, (2018) extended the work of Tay et al (2017b) employing Galilean decomposition, swirling strength and linear stochastic estimation techniques to provide insight into the turbulent structure of the surface jet. They reported a suppression effect of the free surface on the growth of the spanwise vortex cores. Clockwise and counter-clockwise rotating spanwise vortex cores were revealed in the lower and upper shear layers, respectively. Mean swirling strength peaked at the edges of the shear layers with decreasing magnitude as the jet evolved downstream.

Essel and Tachie (2018) investigated the effect of offset height ratio and boundary condition (free surface and solid wall) on the characteristics of submerged twin round jets. They observed that with increasing offset height and downstream distance, the size of the structures was enhanced. Along the center plane of both jets, the growth of the scales was independent of the boundary conditions. However, significant differences were observed in the immediate vicinity of the boundaries. For example, the damping effect on the transverse extent of the surface normal two-point correlation function was stronger close to the solid wall than observed near the free surface.

2.4 Previous Investigations on Turbulent Twin Jets

Investigations into twin jets have predominantly focused on free twin jets which can be viewed as the simplest configuration of multiple jets but with flow dynamics that are relatively more complex than the single jet owing to the interaction between the individual jets. Over the years, there has been considerable effort to understand the characteristics of twin jets (Tanaka 1970, 1974; Ko and Lau 1989; Lin and Sheu 1990; Durve et al. 2012; Harima et al, 2005; Meslem et al, 2010; Zang and New 2015; Laban et al. 2019; Aleyasin and Tachie 2019). These studies focused on both two-dimensional (2-D) flow, otherwise known as plane jets, and three-dimensional (3-D) jets. Three-dimensional jets present more complex flow dynamics because of the interaction of the jets with the ambient fluid in both the spanwise and transverse directions. One important difference between the 2-D and 3-D flow is the presence of a negative streamwise velocity (recirculation) in the converging region of twin plane jets and its absence in 3D jets (Aleyasin & Tachie, 2019).

2.4.1 Two-dimensional turbulent twin jets

Tanaka (1970) investigated the effect of separation ratio between two plane jets, ranging between $8.5 \leq G/W \leq 26.3$ where W is the nozzle width. The experiments were conducted at an exit Reynolds number range of $4{,}290 \leq R_e \leq 8{,}750$. The results revealed an attraction between both jets. This attraction is a consequence of a sub-atmospheric static pressure zone formed between the jets, and results in the converging of the inner shear layers of both jets at a point known as the merging point (M_p). From the experimental results, the following is the correlations between the merging point and nozzle separation:

$$M_p/W = 5.06(G/W)^{0.27} \qquad \text{for} \qquad G/W < 16 \tag{2.7}$$

$$M_p/W = 0.667(G/W) \qquad \text{for} \qquad G/W > 16 \tag{2.8}$$

In a subsequent publication (Tanaka, 1974), the combined region of the plane jets was examined. Relevant observations from this subsequent study are summarized as follows: (I) Velocity profiles of the combined jet are similar, regardless of the nozzle separation ratio and downstream distance along the symmetry plane between the jets; (II) Profiles of turbulence intensities show a clear distinction between the single jet and combined jet, irrespective of separation ratios. For $G/W > 16$, the generation and dispersion of turbulence are not in an equilibrium state; (III) The absolute value of static pressure decreases in the flow direction and the profiles are similar, irrespective of nozzle separation ratio and downstream distance along the symmetry plane between the jets; (IV) The spread of the combined jet increases linearly with the downstream direction but at a higher rate compared to a single jet and also with increasing separation ratio. The following correlations between the spread rate, K_s, and the nozzle separation ratio were proposed:

$$K_s = 72.9(G/W)^{-1} \qquad \text{For} \quad G/W < 16 \tag{2.9}$$

$$K_s = 4.8 \qquad \text{For} \quad G/W > 16 \tag{2.10}$$

(V) Combined jet possesses a higher decay rate, K_d, compared to a single jet and increases linearly with the separation ratio as described by equation (2.11)

$$K_d = 0.055(G/W) \qquad \text{For} \quad G/W > 12 \tag{2.11}$$

The increased decay and spread rates of twin plane jets suggest a superior mixing in comparison to a single jet.

Flow structures in the initial region of twin plane jets were investigated by Ko & Lau (1989). The inner and outer mixing regions of each jet revealed two trains of vortical coherent structures with clockwise rotation (prograde) and anti-clockwise rotation (retrograde) in the inner and outer mixing regions respectively. Successive initial vortices in the inner mixing region undergo either a pairing or an amalgamation process, which respectively resulted in nearly circular or elongated structures.

In the investigation of twin plane jets by Lin & Sheu (1990), reverse flows were observed in the converging region. The mean velocity approached self-similarity in both the converging and combined regions of the flow while turbulence intensities and Reynolds shear stress approached self-similarity in the combined region. Velocity decay and jet spread rates in the combined region are higher compared to a single jet, in agreement with Tanaka (1974). The dependence of the merging point on the separation ratio was represented by the correlation shown in equation (2.12).

$$M_p/W \approx 0.48(G/W) + 8.98 \qquad \text{For} \qquad G/W > 30 \tag{2.12}$$

In the numerical investigation of twin plane jets, Durve et al. (2012) stated a prediction accuracy of $\pm 12\%$ for equation (2.12), but that the correlation was invalid for $G/W < 30$. They proposed a correlation (equation 2.13) that not only depends on the separation ratio but also on the jet exit condition such as turbulence intensity (*I*). This correlation, developed from regression analysis of experimental data in the literature, showed a better prediction of merging points. Similarly, they proposed equation (2.14) for the prediction of the combined point.

$$M_p/W = 0.721(G/W) + 2.06(I) - 2.453 \tag{2.13}$$

$$C_p/W = 1.231(G/W) + 2.06(I) - 2.453 \tag{2.14}$$

2.4.2 Three-dimensional turbulent twin jets

On three-dimensional twin circular jets studies, Okamoto et al., (1985) reported that at a Reynolds number of 230,000 and nozzle separation ratios of 5 and 8, the location of the maximum velocities deflected from the nozzle centerline towards the symmetry plane. The decay of these velocities agreed with that of a single jet. In the outer shear layer, a reduced spread of twin jets compared to the single jet was observed but in the inner shear layer, the twin jets showed a slightly higher spread rate. They compared the twin jets to a jet parallel to a wall, on the principle of the reflected image, where the wall plane becomes the symmetry plane of the twin jets. They concluded that the nature of a boundary condition influences the jet dynamics. Additionally, the effect of nozzle separation ratios ($G/d = 2, 4$ and 8) on twin round jets at $R_e = 25{,}000$ were investigated by Harima et al. (2001, 2005). Unlike plane twin jets, no distinct reverse flow was observed. A reduction in separation ratio resulted in reduced entrainment and a lower decay rate in the combined region, and also a lower decay rate compared to a single round jet. A higher separation ratio shifts the combined points and location of maximum turbulence intensity further downstream. The interaction between both jets suppressed the magnitude of the turbulence intensity and Reynolds shear stress.

Furthermore, the effects of nozzle geometry on single and twin jets produced from circular and non-circular (cross) nozzle geometries were investigated by Meslem et al. (2010). The investigations were conducted at a fixed nozzle separation ratio of $G/d_e = 2.7$ (where d_e is the equivalent diameter of the nozzle). Within a downstream distance of $2 \leq x/d_e \leq 30$, twin jets showed enhanced mixing over the single jet and non-circular geometry over circular, owing to higher entrainment, decay and spread rates, which were in contrast with observations made by Harima et al. (2001).

Twin round jets were investigated by Zang & New (2015), with emphasis on the effects of nozzle separation ratios ($G/d = 1.5,\ 2$ and 3). Mean velocity and turbulent kinetic energy distributions showed enhanced interaction between the jets' shear layers as the separation ratio decreased. Frequency analysis of the shear layers revealed two distinct frequency peaks, which were associated with vortex formation in the outer and inner shear layers. Regardless of the separation ratio, the formation frequency in the outer shear layer remained consistent and similar to that of a single jet. In the inner shear layer, on the other hand, the vortex formation frequency decreased with decreasing separation ratio and was generally lower than the formation frequency in the outer shear layer. POD analysis within a streamwise distance of $0 \leq x/d \leq 8$ revealed that the mechanism governing vortex formation and dynamics were significantly different for $G/d \leq 2$ and $G/d \geq 3$.

Recently, Laban et al. (2019) investigated the effects of separation ratios on the mean and higher-order turbulent statistics of twin round jets produced from a sharp contraction nozzle. In line with the previous findings by Zang & New (2015), it was observed that a reduced separation ratio enhanced the interactions between the jets, reduced jet velocity decay and resulted in reduced levels of Reynolds stresses in the inner shear layer. They concluded that downstream of the potential core, reduced separation ratio resulted in a significant rise in the vorticity thickness, streamwise and transverse turbulence intensities, while the potential core length, streamwise mean velocity and turbulence intensities along the jet centerline were independent of separation ratios. These findings were further supported in a Reynolds number investigation ($R_e = 5{,}000 - 20{,}000$) of twin round jets by Aleyasin & Tachie (2019) who reported increased Reynolds stresses, turbulent kinetic energy production and structure interactions in the inner shear layers, within the converging region. These increases were associated with relatively stronger prograde structures, as revealed by the swirling strength analysis. The three-dimensional twin round jets study by Aleyasin & Tachie (2019), conducted at $R_e = 5{,}000 - 20{,}000$ and nozzle separation ratio of 2.8 also revealed that the combined point locations, as well as velocity decay and spread rates, were Reynolds number independent beyond $R_e = 10{,}000$.

2.5 Previous Investigations on Submerged Jets

One of the earliest studies of submerged jets was performed by Evans (1955) who experimentally investigated the mechanism responsible for stopping waves. He showed that horizontal surface currents were responsible for calming waves and that the required surface current velocity depended on the water depth, current thickness and the wave's length and height. Later, Rajaratnam and Humphries (1984) reported mean streamwise velocity measurements in three surface jet configurations: plane surface jet and surface jets produced from circular and rectangular nozzles. The plane surface jet was mounted flush with the free surface and the experiments were conducted at Reynolds numbers ranging from 686 to 1,431. They observed no significant differences in the decay and spread of the jets at the investigated Reynolds numbers. Comparison of the plane surface jet with the plane free jet showed comparable jet decay rate and a 28% reduced spread rate. For the circular jet, same vertical growth rate as the circular wall jet was reported but at a less than half the growth rate in the transverse direction compared to that of the circular wall jet.

Anthony and Willmarth (1992) conducted mean velocity and turbulence intensity measurements in a submerged round jet at a Reynolds number of 12,700 and an offset height ratio, $h/d = 2$ using a three-component laser Doppler velocimetry (LDV). As the free surface is approached, the surface-normal turbulence intensity decreased while the streamwise and spanwise turbulence intensities increased. These phenomena were attributed to the redistribution of the turbulent kinetic energy.

The effects of exit Reynolds number (Walker et al. 1995; Wen et al. 2014a; Rahman and Tachie 2018), nozzle geometry (Tay et al. 2017a; Rahman et al. 2019) and offset height (Madnia and Bernal 1994; Ead and Rajaratnam 2001; Tsunoda et al. 2006; Sankar et al. 2008; Shinneeb et al. 2011; Wen et al. 2014b; Tay et al. 2017b; Rahman et al. 2018; Essel and Tachie 2018) on the downstream development and dynamics of submerged jets have been examined in considerable detail.

Walker et al. (1995) examined the influence of Reynolds numbers ($R_e = 12{,}700$ and $102{,}000$) and Froude numbers ($Fr = 1 - 8$) on the structure of turbulence in a submerged jet. In the presence of the free surface, high Reynolds number jet evolves slower than the low Reynolds number jet with downstream distance. Transfer of energy from the surface-normal velocity fluctuation to the streamwise and spanwise velocity fluctuations increases with downstream distance. With decreasing Froude number, two-third and one-third of the extracted energy from the surface-normal velocity fluctuation is transferred to the streamwise and spanwise velocity fluctuations, respectively.

The effect of Reynolds number on the interaction of single and twin jets with the free surface was investigated by Rahman and Tachie (2018) using a particle image velocimetry (PIV). The range of Reynolds numbers investigated spanned $2{,}300 \leq R_e \leq 11{,}900$, at a fixed offset height ratio of 2 and nozzle separation ratio of 2.6 for the twin jets. The results showed no significant Reynolds number effects on the potential core length of both the single and twin jets for $R_e \geq 3{,}700$. Similarly, the merging point in the case of twin jets obtained from mean velocity contour plots, showed no significant dependence on R_e. Regarding the attachment length, no significant Reynolds number effects were observed for the single jet for $R_e \geq 3{,}700$ and for the twin jets, for $R_e \geq 3{,}890$. Generally, the twin jets showed a stronger jet-free surface interaction compared to the single jet. Meanwhile, the surface velocity measurements are independent of the Reynolds number in the interaction region ($x/d > 9$) of the twin jets and in the case of the single jet, they are independent of Reynolds number for $R_e \geq 3{,}700$. The surface velocity increased at a 55% slower rate at $R_e = 2300$. For $R_e \geq 3{,}700$, no significant influence of Reynolds number on the entrainment coefficient, as well as the decay and spread rates, were observed. Furthermore, the submerged jets decayed at a slower rate compared to free jets due to the limited available ambient fluid for entrainment.

The effects of nozzle geometry were investigated in a single submerged jet at an offset height ratio of 2.7 by Tay et al. (2017a**)** and at a Reynolds number of 7,900. The jets were produced from a square nozzle and rectangular nozzles with aspect ratios of 2 and 4. A 7% and 3% higher decay rates over the square jet was reported for the aspect ratios of 2 and 4 (oriented in the minor axis of the jet) rectangular jets, respectively. Re-orienting the aspect ratio of 4 nozzle from the minor to the major axis reduced the decay rate by 8%, relative to the square. The spread of the lower shear layer of the square nozzle closely compares with that of the aspect ratio of 4 (major orientation) rectangular nozzle while the aspect ratio of 2 and 4 (minor orientation) spreads at 14% and 42% higher rates, respectively, when compared to the square nozzle. However, the turbulence intensities, Reynolds shear stresses and structure parameter were nearly independent of the aspect ratios.

More recently, Rahman et al. (2019) investigated three nozzle geometries: circular, square and rectangular nozzle with an aspect ratio of 3. The equivalent exit area of each nozzle was 11.3 mm, and the measurements were performed at a fixed Reynolds number of 5,500 and an offset height ratio of 2. For the rectangular nozzle, measurements were performed in both the minor and major planes. Employing Galilean decomposition and swirling strength techniques, instantaneous visualizations of the flow field showed the largest enhancement and near field mixing in the minor orientation of the rectangular nozzle when compared to the circular, square and rectangular (major orientation) nozzles. The mean velocity contours revealed a 33% reduction in potential core length in the non-circular nozzles, relative to the circular nozzle. In the major axis orientation, the rectangular jet increased the potential core length by about 33% relative to the minor axis. The attachment lengths of the round and square nozzles are similar, but 33% longer than the minor oriented rectangular nozzle. Re-orienting the rectangular nozzle from the minor plane to the major plane showed a 60% increase in attachment length. The rapid expansion in the rectangular jet in the minor axis resulted in the fastest deflection of the jet towards the free surface and fastest decay rate of the maximum streamwise mean velocity. Within $5 \leq x/d \leq 18$, the minor oriented rectangular jet decayed by 40% over the circular jet and by 35% over the square and major oriented rectangular jets. Similar to the jet and free surface interaction reported by Tay et al. (2017a), the minor oriented rectangular nozzles showed enhancement of the free surface strain, shear layer vorticity thickness and damping of the surface-normal velocity fluctuation at the free surface.

Sankar et al. (2008) investigated the effect of offset height effect in a submerged surface attaching jet. They studied a square jet issuing from a smooth contraction square nozzle with measurements obtained at four different offset heights $(h/d = 0.9,\ 1.8,\ 2.7 \text{ and } 4)$. They used a two-component laser Doppler anemometer to perform velocity measurements at five downstream locations $(x/d = 0.4, 1.8, 4.4, 8.9 \text{ and } 13.3)$. It was observed that the jet attachment point moved downstream with increasing offset height. With offset height greater than $1.8d$, a negligible effect of the free surface on velocity profiles was observed. As the offset height increased, increased turbulence activities were reported from the analysis of third-order moments. Results from quadrant analysis clearly showed that the strongest events were less affected by changes in offset height.

Madnia & Bernal (1994) performed an experimental investigation to investigate the interaction of a turbulent round jet with the free surface. Offset heights of $h = 1d, 1.5d, 2.5d$ and $3.5d$ were studied to elucidate the effects of confinement on the surface jet. Flow visualization and surface curvature measurements were conducted using the shadowgraph technique while velocity measurements were obtained using hot-film probes in both the surface-normal and spanwise directions. They showed that surface deformations were caused by vortex ring-like structures in the flow as they approached the free surface. Also, the point of attachment to the free surface was displaced downstream with increasing offset height.

Wen et al. (2014b) studied a surface jet discharged from a pipe using laser-induced fluorescence (LIF) technique and time-resolved particle image velocimetry for flow visualization and velocity measurements, respectively. The effects of offset height were examined by varying it as $h/d = 2, 4$ and 6. At the offset height ratio of $h/d = 2$, the LIF results showed a near field jet-free surface interaction that resulted in a large-amplitude distortion of the free surface. The resulting downward motion of the free surface revealed a surface-normal compression of the subsurface jet flow. This free surface distortion diminished with increasing downstream distance and offset height. At the offset height ratio of $h/d = 4$, upwelling and downward entrainment motions were observed prior to the jet's attachment to the free surface. After attachment, the structures near the free surface experienced a merging and restructuring process. At $h/d = 6$, the flow field was symmetric prior to attachment and no dynamic changes in the structures were reported after attachment as in the case of $h = 4d$.

In another study, Tay et al. (2017b) characterized the influence of offset height (achieved by varying offset height, $h/d = 1, 2, 3$ and 4) on the structure of a surface jet produced from a square nozzle using particle image velocimetry. The results showed that decreasing the offset height nullifies the turbulent/non-turbulent interface and suppresses structures responsible for entrainment and mixing. This decreased entrainment also results in reduced growth of the jet in the upper shear layer at the near-exit region. The attachment length increased monotonically with increasing offset height when normalized with nozzle width. Meanwhile, when the length scale proposed by Madnia & Bernal (1994), which is the offset height, is used, the attachment length in each test case was observed to be three times the offset height. The decay and spread rates also increased with increasing offset height. The free surface flow was described to be in a state of strain due to the acceleration and subsequent deceleration of surface velocity. Additionally, the magnitude of the velocity decreased with increasing offset height. A reduction in offset height increased turbulence intensity levels at the free surface.

The experimental investigation by Essel and Tachie (2018) was the first extensive investigation into submerged twin jets. The study aimed to characterize the effects of offset heights $(h/d = 1, 2, 3 \text{ and } 4)$ and boundary conditions (free surface and solid wall) on the mean flow properties and turbulence characteristics of round twin jets. Using a PIV, at a fixed Reynolds number and nozzle separation ratio of 5,000 and 2, respectively, they reported the following observations: (I) An increasing combined point distance with decreasing offset height ratio, irrespective of boundary condition. However, the locations of the combined point in the wall-bounded case were 16% longer than in the free surface bounded case; (II) For jets closer to the boundaries, two stages of decay rates were reported and the two stages were independent of boundary condition. Furthermore, the second stage decay rates were independent of offset height ratios; (III) Damping effect on surface-normal turbulence intensity and Reynolds shear stress by the boundaries was more dramatic for the solid wall due to the no-slip condition; and (IV) Enhanced large-scale anisotropy and negligible structure parameter near the boundaries were observed, suggesting the likelihood of turbulence models that do not solve for various Reynolds stresses to inaccurately predict flow characteristics in the immediate vicinity of the boundaries.

CHAPTER THREE

EXPERIMENTAL SETUP AND MEASUREMENT PROCEDURE

In this chapter, the description of the experimental setup, test conditions, and measurement procedure, as well as uncertainty estimates are presented. The principle of operation of the PIV system and its various components are also discussed.

3.1 Experimental Setup

Figure 3.1 shows the schematic diagram of the open recirculating water channel used in this experiment. The test section measures 2500 mm in length, 200 mm in width and 200 mm depth. The sides and bottom of the test section are made of transparent acrylic plates for optical access. The flow was driven by a variable speed centrifugal pump through a flow-conditioning unit and then into a 6.5:1 converging section. The resulting fine-scale flow passes through the nozzle assembly, mounted 100 mm from the channel exit. The jet is produced from nozzle plates mounted on the nozzle assembly. The nozzle plate is made from 3 mm thick acrylic material, screwed onto the nozzle assembly, and designed to provide a sharp-edged orifice type nozzle. The Cartesian coordinate system is adopted with x, y and z (not shown) aligned to the streamwise direction, free surface – normal direction and spanwise direction, respectively. The $x = 0$ location is at the jet exit and $y = 0$ is at the mid-point between both nozzles (otherwise known as the symmetry plane). As shown in the figure, the center of the upper jet, identified as Jet A is at an offset height of h from the free surface while the lower jet (Jet B) is at an offset height of H from the wall. The separation between the two nozzles is represented by a distance G. A weir was installed downstream of the jet exit, precisely at 2300 mm to regulate and maintain a constant water depth within the test section. See Fig. 1.1 for the definition of variables.

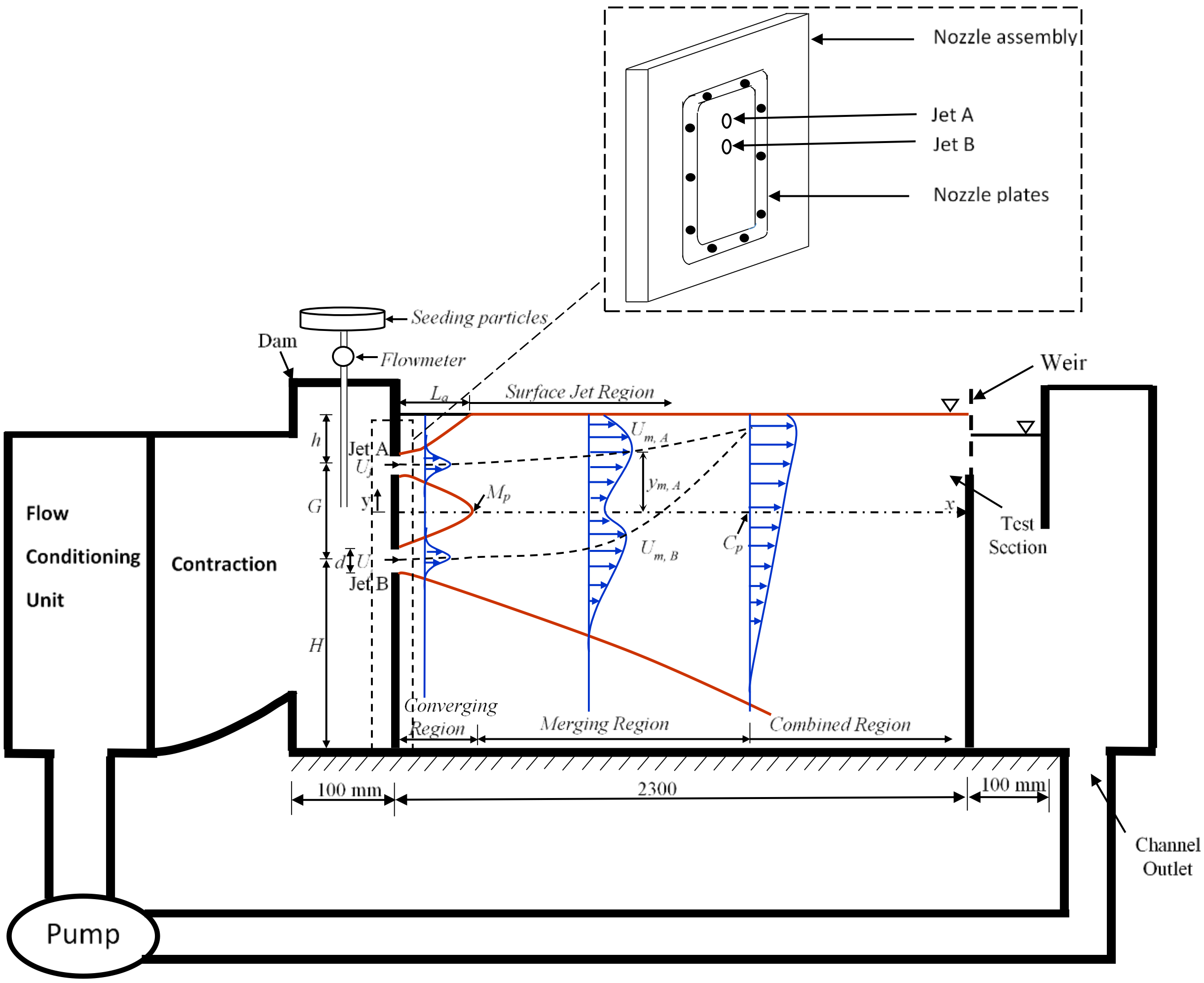

Figure 3. 1 Schematic of the water channel (not to scale)

3.2 Experimental Test Conditions

The experiments were performed using three different nozzle geometries: round, square, and rectangle (aspect ratios of 0.3 and 3) at fixed separation ratio of $G/d = 2.3$, and Reynolds number,

$R_e = U_j d_e/\upsilon = 4{,}400$. The choice of $R_e = 4{,}400$ is based on Reynolds number independence at $R_e \geq 3{,}890$, reported by Rahman and Tachie (2018) and to ensure that the free surface is relatively calm, to facilitate high-quality data close to the free surface. To allow for strong jet-free surface interaction and for the observation of the pre-attachment region, an offset height of $h = 2d$ was chosen and $H \approx 21d$ was selected to minimize the channel bed effect on the flow dynamics. The nozzle arrangements studied are shown in Fig. 3.2, with the dimensions provided in Table 3.1. It should be noted that, for the rectangular nozzle, measurements were performed in both the minor and major planes. The dimensions of the non-circular geometries correspond to the circle-equivalent diameter, $\left(d_e = \sqrt{4A/\pi}\right)$ of approximately 8 mm, where A is the jet exit area.

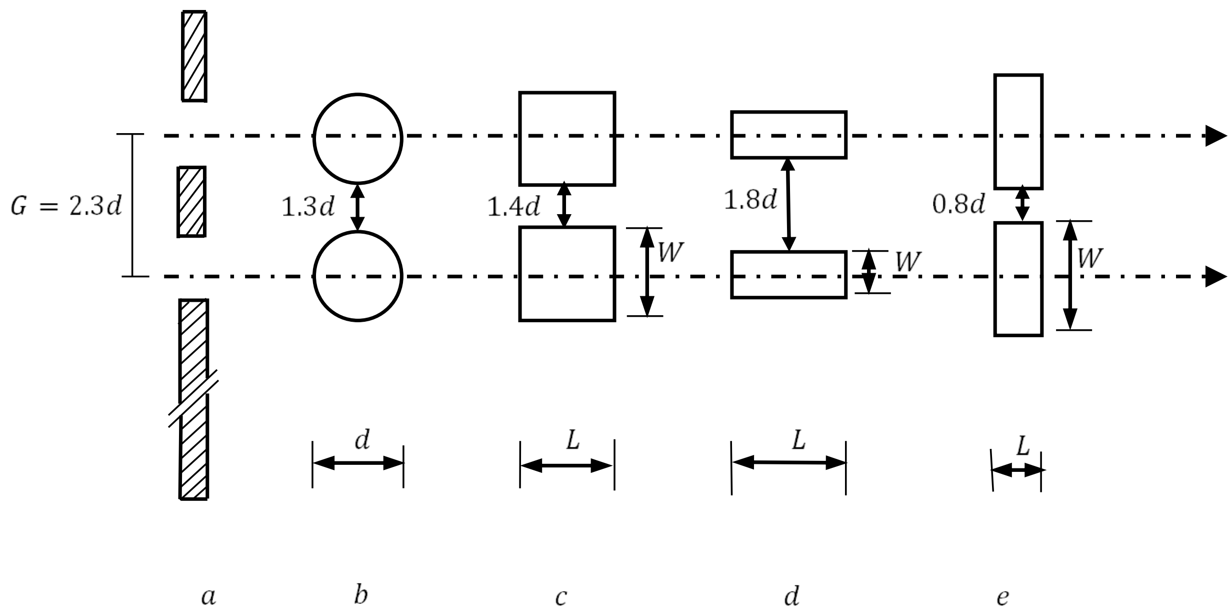

Figure 3. 2 Schematic diagrams of the nozzle type and geometry arrangements investigated. (a) Orifice nozzle (b) Round geometry (c) Square geometry (d) Rectangular geometry (minor orientation) (e) Rectangular geometry (major orientation)

Table 3. 1 Nozzle geometry dimensions

Geometry	Dimensions		
	d	L	W
Round	$8\ mm$	-	-
Square	-	7.07 mm	7.07 mm
Rec_min	-	12.1 mm	4.14 mm
Rec_maj	-	4.14 mm	12.1 mm

The summation of the cross-sectional area of both nozzles in each case ($\approx$ 100 mm^2) and the Reynolds number were chosen to ensure that the jets discharged with the same momentum flux and to facilitate comparison with both single and twin jet studies in the literature.

3.3 PIV System and Measurement Procedure

Particle image velocimetry is an optical, non-intrusive technique that provides simultaneous whole-field instantaneous velocity measurement. For this study, the planar PIV was used and the basic principle of operation is discussed here. The experimental setup is as shown in Fig. 3.3 and consists of a pulsed laser light source, charged coupled device (CCD) camera, a synchronizer (timer hub) and a data acquisition system (computer). Also, the flow is seeded with particles that illuminate the laser light.

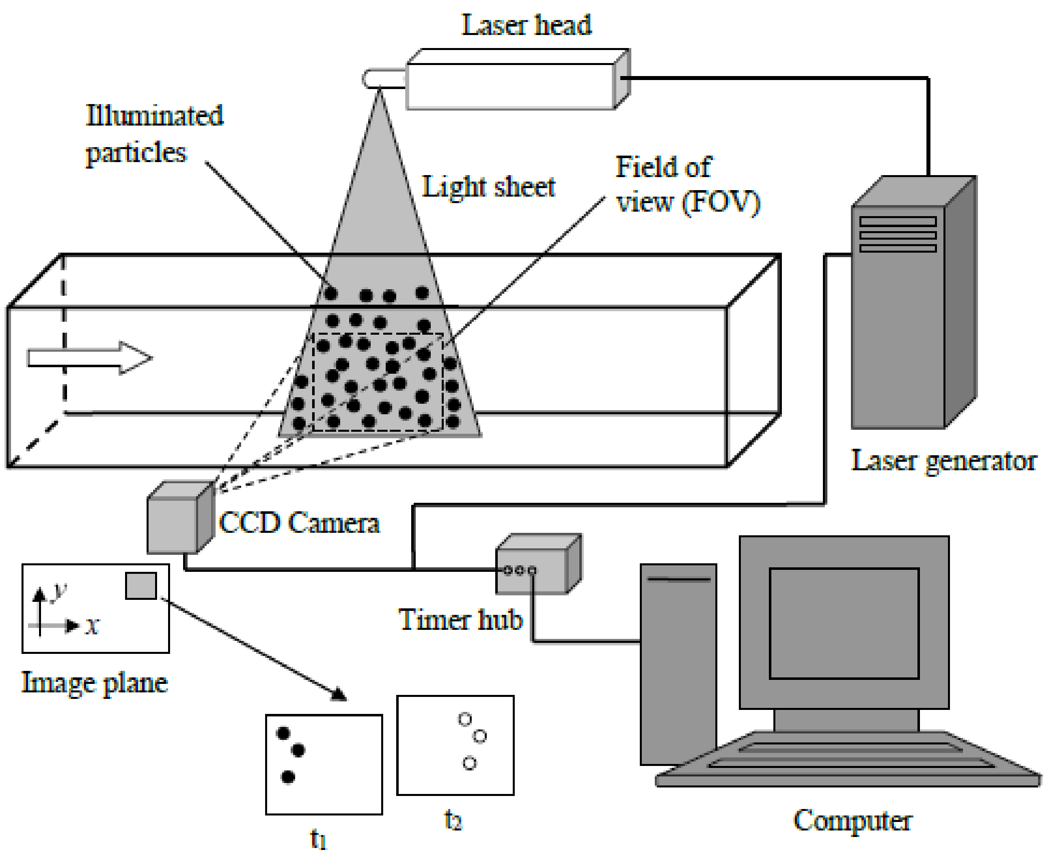

Figure 3. 3 Experimental setup of planar PIV (Rahman, 2019)

The principle of operation is described as follows. Fluid flow is passed through an optically transparent test section (as shown by the arrow sign) and is seeded with light-scattering particles. A double pulsed laser sheet, separated by a time delay, Δt, illuminates the flow field at times t_1 and t_2. As the light impinges on the particles, the particles scatter the light and the CCD camera captures and records the images within the field of view (FOV) either on a single frame or on two separate frames. With the help of a computer program, these images are subdivided into grids of smaller areas known as interrogation areas (IA). Depending on the number of recorded frames, auto-correlation or cross-correlation algorithms are applied to each interrogation area to statistically determine the local displacement vector, $\overrightarrow{\Delta x}$, of the particles between the first and second illuminations. The velocity vector is then calculated from the following expression: $\vec{V} = \overrightarrow{\Delta x}/\Delta t$. Subsequent correlation of all interrogation areas within the FOVs produces the velocity vector map for each image pair. An overview of the basic components of the PIV is presented below.

3.3.1 Seeding Particles

From the foregoing, it is evident that the PIV measures the velocity of the seeding particles and not the fluid velocity. As such, to ensure an accurate representation of the fluid velocity, the seeding particles should possess certain properties to avoid significant discrepancies between the fluid and particle motions. Furthermore, they should be homogeneously distributed within the flow, small enough to faithfully follow the flow but large enough to scatter sufficient light that is visible to the CCD camera. The flow tracking capability of the seeding particles is characterized by its response time, settling velocity and Stokes number (Raffel et al. 2007). Particle response time is the measure of the tendency of the particle to attain velocity equilibrium with the fluid (Agelin-chaab, 2010) while the settling velocity is a measure of the velocity lag between fluid and particle velocities. It is evaluated from equation (3.1) (Raffel et al. 2007):

$$\tau_r = \rho_p \frac{d_p^2}{18\mu_f} \tag{3.1}$$

where d_p is the diameter of the particle, μ_f is the fluid viscosity and ρ_p is the density of the particle. According to Mei et al. (1991), settling velocity can be estimated from equation (3.2)

$$V_s = \frac{(\rho_p - \rho_f) g d_p^2}{18\mu_f} \tag{3.2}$$

where ρ_f is the density of the fluid and g is the acceleration due to gravity. On the other hand, the Stokes number is evaluated from equation (3.3)

$$St = \frac{\tau_r}{\tau_f} \tag{3.3}$$

where τ_r is the particle response time and τ_f is the fluid time scale (time between laser pulses).

Hence, from the equations above, particle diameter and density influence the flow tracking capability of seeding particles. This implies that particles with minimal settling velocity should ideally be of sufficiently small diameter and density that is close to the density of the working fluid. From commercially available seeding particles, a $10\mu m$ silver-coated hollow glass sphere with a specific gravity of 1.4 was chosen for this study and filtered water as the working fluid. Based on these, the particle response time, settling velocity and Stokes number were estimated to be $7.78 \times 10^{-6} s$, $2.18 \times 10^{-5}\ m/s$ and 0.003, respectively. These values are satisfactory as the particle response time is very small compared to the sampling time for this experiment. Similarly, as particles with negligible settling velocity is desirable, the present value is insignificant as it is up to four order of magnitude smaller than the measured streamwise mean velocity. A Stoke number, $St < 0.1$ suggests the ability of the seeding particles to follow the fluid flow faithfully and hence, approximates the fluid velocity with an error less than 1% (Tropea et al. 2007). Therefore, an $St\ = 0.03$ is satisfactory.

3.3.2 Laser Light Source

Neodymium-yttrium-aluminum-garnet (Nd:YAG) double-pulsed laser which provides monochromatic light with high intensity was used in this study. The emitted laser light passes through a system of lens to produce a 1 mm light sheet thickness (to reduce the number of de-focused particles) that illuminated the field of view with a maximum energy of 120 mJ per pulse and 532 nm wavelength. The time delay between illumination pulses was determined to ensure the one-quarter displacement rule was observed (Keane & Adrian, 1990). This was done to minimize the out-of-plane motion of particles and to obtain a good signal-to-noise ratio (Agelin-chaab, 2010). The time delay between pulses was determined from equation (3.3)

$$\Delta t = \frac{IA \times d_{pitch}}{4 M_f U_{max}} \tag{3.3}$$

where IA is the interrogation area size, d_{pitch} is the pixel pitch, M_f is the magnification factor and U_{max} is the maximum velocity of the flow.

3.3.3 Recording Medium

A 12-bit charge-coupled device camera with a resolution of 2048 pixel $\times 2048$ pixel and a pixel pitch of $7.4\ \mu m$ captured the reflected light from the seeding particles. The camera is HiSense 4M and coupled to a 60 mm AF Micro Nikkor lens. The camera has high-performance progressive scan interline CCD chips with equal arrays of photosensitive and storage cells. The mode of operation of this camera is such that the first captured image resulting from the first pulse trigger is transferred immediately from the photosensitive cells to the storage cells and the image capture from the second laser pulse is stored directly on the photosensitive cells. This allows for a sequential transfer of the images from the camera to the computer storage for processing. The field of view of the camera was set to 110 mm $\times 110$ mm and measurement was acquired in two overlapping planes (50% overlap) in the streamwise direction spanning $0 \leq x/d \leq 25$ from the jet exit. Based on a convergence test (not shown), 5000 image pairs were acquired in each measurement plane at an acquisition rate of 4 Hz.

3.3.4 Data Post Processing

The instantaneous digital images recorded by the camera are post-processed using a cross-correlation algorithm to determine particle displacements within the interrogation area. The algorithm used in this study is the adaptive correlation option provided by the DynamicStudio version 4.1. This advanced cross-correlation algorithm uses a multi-pass fast Fourier transform (FFT) algorithm with a one-dimensional Gaussian peak-fitting function (Rahman et al. 2018). The interrogation area size was initialized as $128\,\text{pixels} \times 128\,\text{pixels}$ with a 50% overlap and finalized as 32 pixels $\times 32$ pixels with a 50% overlap in both the x and y axes. This resulted in an 8-pixel maximum particle displacement, in keeping to the one-quarter particle displacement rule (Markus Raffel et al., 2007).

3.4 Uncertainty Estimates

Following the standards prescribed by the American Institute of Aeronautics and Astronautics, a measurement uncertainty analysis was carried out. The standard was described by Coleman and Steele (1995), and it involves the identification and quantification of all error sources. Generally, precision and bias errors constitute major components of the total error in experimentally determined results. Sources of error in a PIV could be from pulse-separation time selection, insufficient sample size, and spatial resolution effect. Prasad et al (1992) and Forliti et al (2000) presented a detailed analysis of precision and bias errors in a PIV. In this study, uncertainties in the mean velocities, turbulence intensities, and Reynolds stresses at 95% confidence level were estimated to be $\pm 3\%, \pm 7\%, \text{and } \pm 10\%$ of their local peak values, respectively.

CHAPTER FOUR

RESULTS AND DISCUSSIONS

In this chapter, the effects of nozzle geometry on the mean flow, turbulent statistics and the turbulent structures of surface attaching twin jets are discussed. Mean and turbulent statistics and joint probability density function are used to characterize the flow.

4.1 Flow Visualization

4.1.1 Contours of mean velocities

Iso-contours of the normalized streamwise mean velocity produced from jets of round, square and rectangular minor and major oriented nozzles are shown in Fig. 4.1. It should be noted that the free surface is located at $y/d = 3.2$, irrespective of nozzle geometry. It is observed from the figure that the minor oriented rectangular nozzle shows the greatest expansion of the shear layers. Meanwhile, the shear layers of the rectangular nozzle oriented in the major plane (Fig. 4.1d) show no significant expansion between $0 \leq x/d < 4$. This observation is associated with the axis-switching phenomenon in non-circular jets (Aleyasin et al. 2017a, 2017b). The length of the potential core, L_{pc}, is used to characterize the mixing capability of jets in the near-exit flow region. Following Aleyasin et al. (2017a), the length of the potential core is defined as the streamwise distance from the jet exit plane to the point where the centreline velocity decays to 98% of its maximum. The average potential core length of the twin jets produced from the various nozzle geometries is presented in Table 4.1. The potential core length for the round and major oriented rectangular jets are similar, however, the square and minor oriented rectangular jets show a 23% reduction in the potential core length compared to the round jet. The potential core length of the square and minor oriented rectangular jets show comparable values with the submerged single jet study of Rahman et al. (2019) while the present round and major oriented jets show a 13% reduced potential core length.

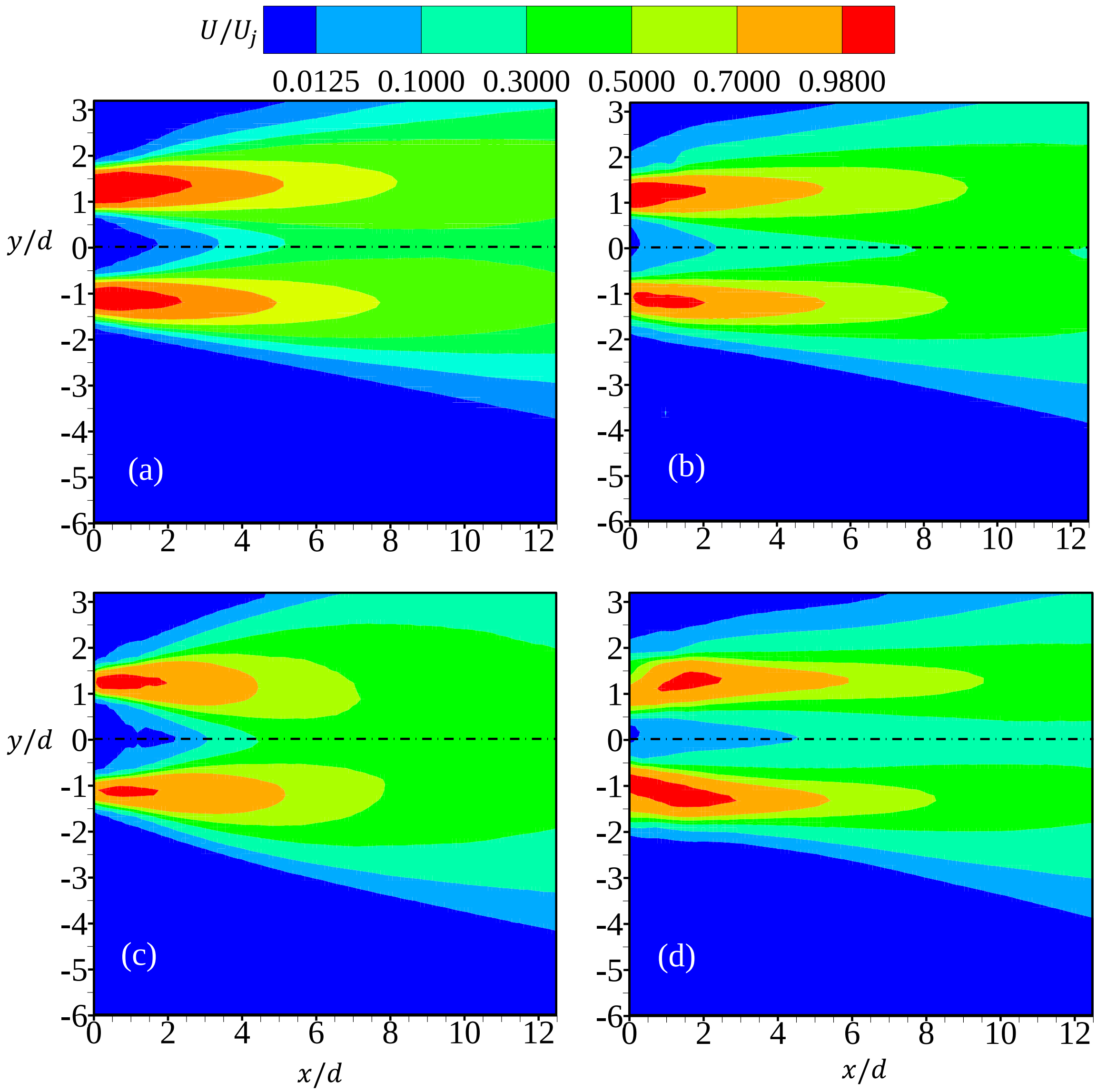

Figure 4. 1 Iso-contour of streamwise mean velocities (a) Round jet (b) Square jet (c) Rect_min jet (d) Rect_maj jet

This suggests that the presence of an adjacent jet in the case of the square and minor oriented rectangular twin jets does not affect near-field mixing. Rahman et al. (2019) also observed that the re-orientation of the rectangular nozzle from the minor plane to the major plane results in reduced near-field mixing. This observation is in agreement with enhanced near-field mixing of square and rectangular (oriented in the minor axis) geometries as reported in free jet studies by Aleyasin et al. (2017a).

Table 4. 1 Potential core lengths (L_{pc}) and attachment lengths (L_a)

Geometry	$\boldsymbol{L_{pc}/d}$	$\boldsymbol{L_a/d}$
Round	2.6	5.2
Square	2.0	5.7
Rect_min	2.0	4.6
Rect_maj	2.6	7.0

From Fig. 4.1, the attachment point (AP) is determined from the contour plot as the point where the minimum streamwise mean velocity contour level, $U/U_j = 0.0125$. The attachment length (L_a) for all geometries are shown in Table 4.1. Jet from minor oriented rectangular nozzle shows the shortest attachment length, in line with the most rapid shear layer expansion and enhanced near-field mixing. The longest attachment length of the major oriented rectangular nozzle is as expected, owing to the delayed shear layer expansion. While enhanced mixing in jets issuing from the minor oriented rectangular nozzle is evident in the 12% and 19% reduction in attachment length over the round and square jets, respectively, re-orienting the rectangular nozzle from minor to major plane shows a 52% increase in the attachment length. Compared to the submerged single jet results of Rahman et al. (2019), twin jets show a reduced attachment length. This could be attributed to strong jet interactions which result in increased ambient fluid entrainment and subsequently, faster expansion of the shear layers.

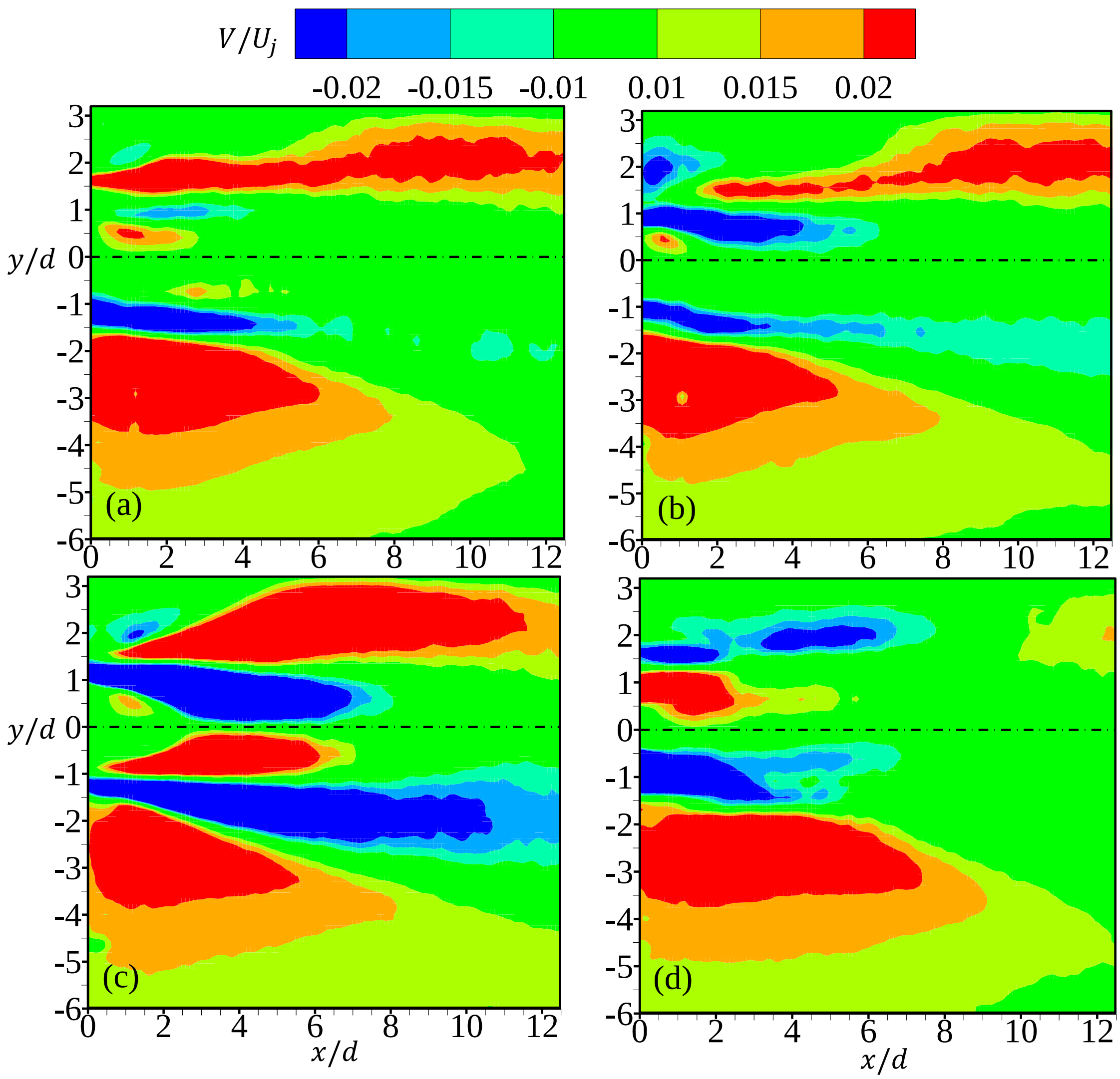

Figure 4. 2 Iso-contour of surface-normal mean velocities (a) Round jet (b) Square jet (c) Rect_min jet (d) Rect_maj jet

Figure 4.2 shows the normalized contours of the surface-normal mean velocities for the different geometries. As evident in Fig. 4.2a, b, and c, negative and positive distributions of the contours are observed in each share layer of both jets. In the upper shear layer of each jet, these represent the ambient fluid entrainment and outward growth of the shear layers, respectively. The reverse is the case in the lower shear layers. The free surface confined the growth of the outer shear layers of Jet A compared to Jet B. A similar trend is observed between the inner and outer shear layers of the twin jets. The rect_min jet shows larger streamwise and surface-normal reach of the contours, consistent with the more rapid growth of the jet as compared to the other geometries. For the rect_maj jet (Fig. 4.2d), negative and positive contour levels are dominant in the outer shear layers of Jets A and B, respectively, while the pattern is reversed in the inner shear layers.

4.1.2 Contours of turbulent quantities

Figure 4.3 shows the iso-contours of the Reynolds shear stress for all four test cases examined. Each jet is characterized by a negative or positive Reynolds shear stress, imitating the direction of the mean streamwise velocity gradient in the shear layers. The greater spatial extent of the contours in the outer shear layers relative to the inner shear layers indicates an enhanced turbulent mixing. The confinement effect of the free surface reduces the spatial extent of the Reynolds shear stress contours in the outer shear layer of Jet A, relative to Jet B. Furthermore, the notion of stronger turbulent mixing in the near field is evident within $0 \leq x/d \leq 8$. Larger regions of Reynolds shear stress in the rect_min jet (Fig. 4.3c), indicative of increased mixing zone, supports enhanced mixing in jets produced from the minor oriented rectangular nozzle. Considering the rect_maj jet (Fig. 4.3d), there is a change in sign within the shear layers, downstream of $x/d = 1$ and closely followed by the convergence and divergence of the jets within $4 \leq x/d \leq 6$. This behaviour is likely a consequence of the axis-switching phenomenon.

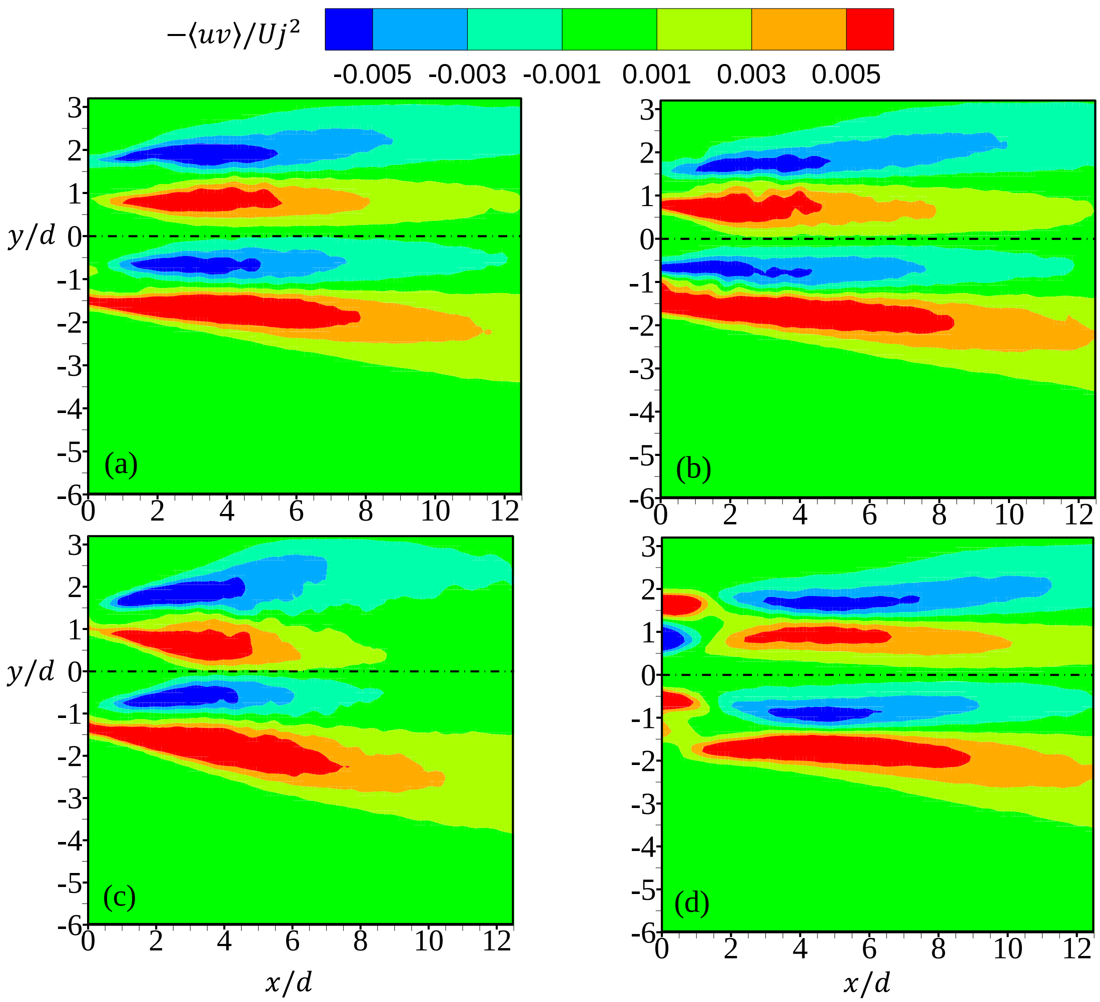

Figure 4. 3 Iso-contour of Reynolds shear stress for (a) Round jet (b) Square jet (c) Rect_min jet (d) Rect_maj jet

Figure 4.4 shows the turbulent kinetic energy contour of the geometries studied. Turbulent kinetic energy is expressed in equation (4.3).

$$k = {}^{1}/_{2}\,(\langle u^2\rangle + \langle v^2\rangle + \langle w^2\rangle) \qquad (4.3)$$

Since a planar PIV was used to obtain velocity measurements in this investigation, only the streamwise and surface-normal velocity components were obtained. Based on previous studies of a three-dimensional free jet (Hussein et al. 1994) and submerged jet (Anthony and Willmarth 1992;

Walker et al. 1995), $\langle v^2 \rangle \approx \langle w^2 \rangle$. Hence, equation (4.4) is used to approximate the turbulent kinetic energy.

$$k = {}^{1}/_{2}\left(\langle u^2 \rangle + 2\langle v^2 \rangle\right) \qquad (4.4)$$

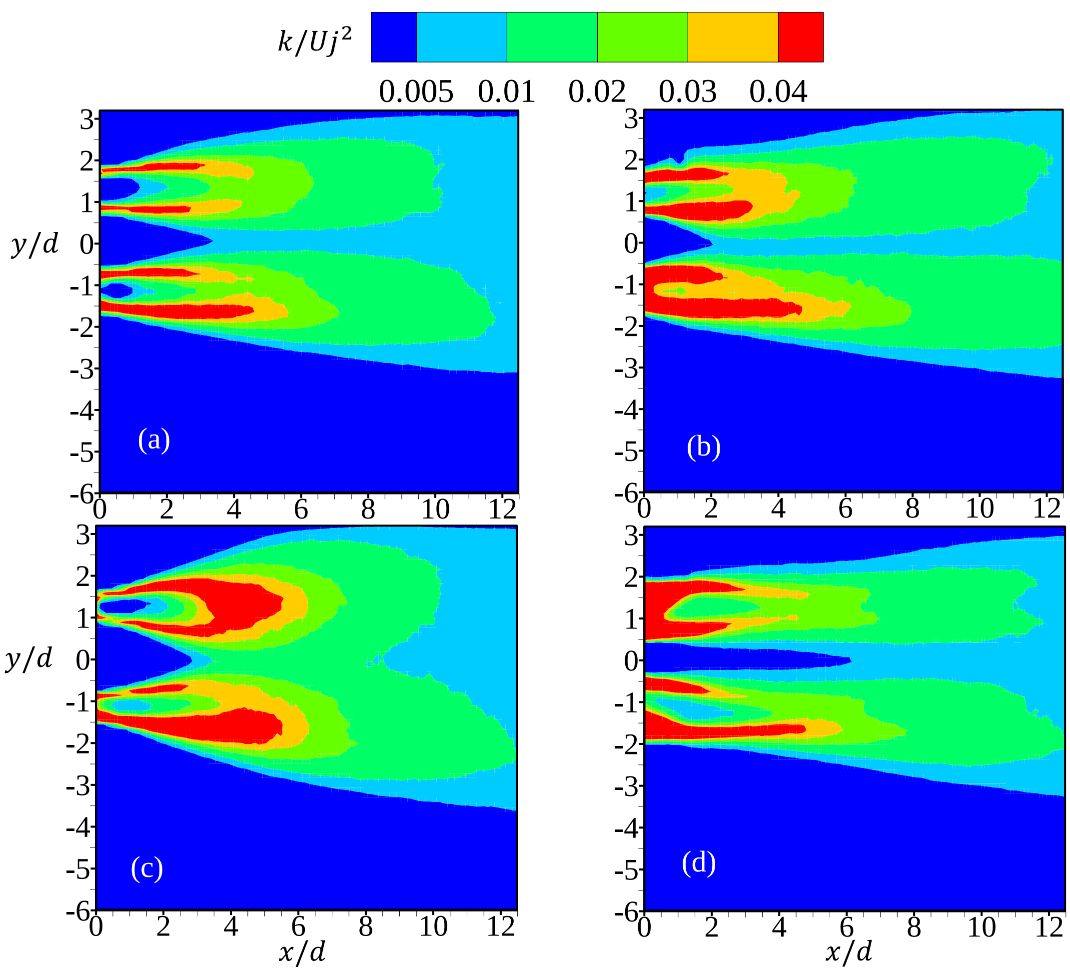

Figure 4. 4 Iso-contour of turbulent kinetic energy for (a) Round jet (b) Square jet (c) Rect_min jet (d) Rect_maj jet

From Fig. 4.4, it is evident that maximum turbulent kinetic energy occurs close to the jet exit. This should be expected because of the high turbulence intensity accompanying the shear layer instability. Rect_minor jet shows the largest extent of turbulent kinetic energy when compared to the other jets.

4.1.3 Contours of the instantaneous velocity field

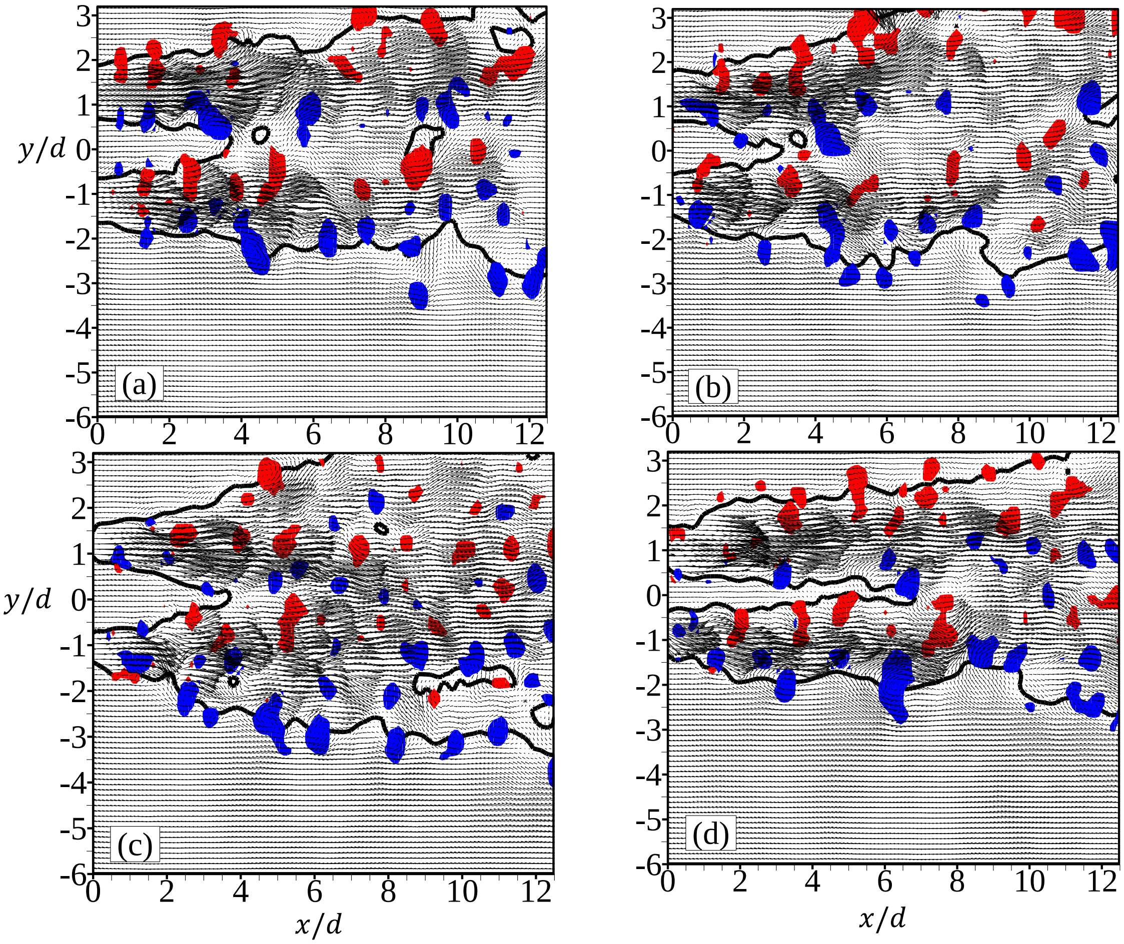

Figure 4. 5 Instantaneous velocity field for (a) Round jet (b) Square jet (c) Rect_min jet (d) Rect_maj jet

Figure 4.5 shows a Galilean decomposition of the instantaneous velocity field, with associated signed swirling strength contours (blue and red patches) of the spanwise vortex cores superimposed on it. Following Agrawal and Prasad (2002), the Galilean transformation was carried out on each instantaneous velocity field by subtracting a constant convective velocity of $0.15U_j$ from the instantaneous streamwise velocity. At the edges of the shear layers where the entrainment process occurs, small-scale vortices that propagated at this convective velocity are revealed. The solid lines, representing the zero velocity contour lines, indicate the centers of the spanwise vortex core that are located at the edges of the shear layer. These lines approximate the interface between the jet and the ambient fluid. The blue and red swirling strength patches are representative of clockwise (prograde) and counter-clockwise (retrograde) rotating vortices, respectively.

The rect_min jets show relatively more vortices that would explain the enhanced interaction between the jets and the ambient fluid and subsequently, faster shear layer expansion. Braid-like structures (darkened patches) observed within $0 \leq x/d \leq 10$ correspond to the vortex rings advancing downstream at this convective velocity. Figure 4.5c shows a relatively earlier interaction of the structures of Jets A and B within $6 \leq x/d \leq 10$ as compared to the round, square and major oriented rectangular nozzle jets. After the attachment point, the absence of the swirling strength due to the presence of the free surface is observed.

4.2 Streamwise Evolution of Local Mean Velocity and Half-Velocity Width

4.2.1 Mixing and combined point

As shown in Fig. 1.1, twin jets can be divided into three distinct regions: converging region, merging region, and combined region. Various methods have been used in the literature to identify these regions. In twin plane jets, the point where the negative streamwise velocities along the symmetry plane no longer exist and the velocity becomes zero identified the merging point (Durve et al., 2012; Tanaka, 1970). For the three-dimensional twin jets examined in the present study, this method is not applicable because of the absence of negative streamwise velocities. For a three-dimensional jet, previous investigations (Harima et al., 2001; Vouros and Panidis 2008; El Hassan and Meslem 2010; Ghahremanian et al., 2014) identified the merging point as the location where the velocity along the symmetry plane reached 10% of the local maximum velocity. Based on the foregoing definition, the merging point in this study is identified as the location along the center plane between Jets A and B, where the local minimum velocity is 10% of the local maximum velocity, and the results are presented in Table 4.2. Considering measurement uncertainty of the merging point, $x_{Mp} = \pm 0.5d$, it is observed from the table that the round, square and rect_min jets show comparable merging points. This appears to be in contradiction to the faster shear layer expansion of the rect_min as seen in section 4.1. To explain this variation, consider the distance between the base of nozzle A and the top of nozzle B (herein referred to as end-to-end separation) as shown in Fig. 3.2. The rect_min nozzles show the largest separation between the twin nozzles. This shows that the largest end-to-end separation of the twin rect_min nozzle accounts for the delayed merging point when compared to the round and square nozzles. Despite the increased end-to-end separation of the rect_min nozzle, the comparable merging point location with the round and square nozzle is a testament to the faster growth of the shear layers.

Table 4. 2 Locations of Merging and Combined points

Geometry	**Merging point, $\boldsymbol{Mp\ (x_{Mp}/d) \pm 0.5}$**	**Combined point, $\boldsymbol{Cp\ (x_{Cp}/d)}$**
Round	3	-
Square	2	-
Rect_min	3	18
Rect_maj	4.5	-

The longest merging point of the rect_maj, despite having the least end-to-end separation is because of the axis-switching phenomenon as explained in section 2.1 and in the flow visualization result presented in Fig. 4.1d. Comparing the merging point of the round jet of this study with the twin round free jet of Aleyasin & Tachie (2019) showed a 73% increase in the merging point of the twin round free jet. This difference can be attributed to the different initial conditions such as the nozzle type (linear-contoured nozzle) and nozzle separation ratio ($G/d = 2.8$) as Laban et al. (2019) showed that the merging point increases with increasing separation ratio.

The combined point is used to characterize the transition point from a twin jet to a single jet. In the free jet literature, the combined point is determined as the point where the streamwise velocity on the symmetry plane coincides with the jets' centreline velocity. Due to the asymmetry imposed on the mean flow by the free surface in the submerged jet study, Essel and Tachie (2018) determined the combined point as the streamwise distance where points of inflection disappear from the streamwise mean velocity profile. This method has been adopted in this study. As shown in Table 4.2, only the rect_min jet has a distinct combined point within the streamwise extent of the fields of view which is $0 \leq x/d \leq 25$.

4.2.2 Local maximum mean velocity decay

To characterize mixing, the streamwise evolution of the normalized local streamwise mean velocity of the twin jets issuing from different nozzle geometries is shown in Fig. 4.6. Within $0 \leq x/d \leq 3$, there is negligible decay of the local maximum velocity and this streamwise extent corresponds to the length of the potential core. Downstream of $x/d = 3$, entrainment and interaction between the jets result in the decay of the local maximum velocity which gives an almost linear increase in the U_j/U_m with x/d. The decay rate was estimated by fitting least-squares lines to the U_j/U_m profiles following equation (1.1). For brevity, only the least-squares line fitted to the round jet is shown in Fig. 4.6. Summary of the jets' decay rates and the x/d ranges where they were obtained are presented in Table 4.3.

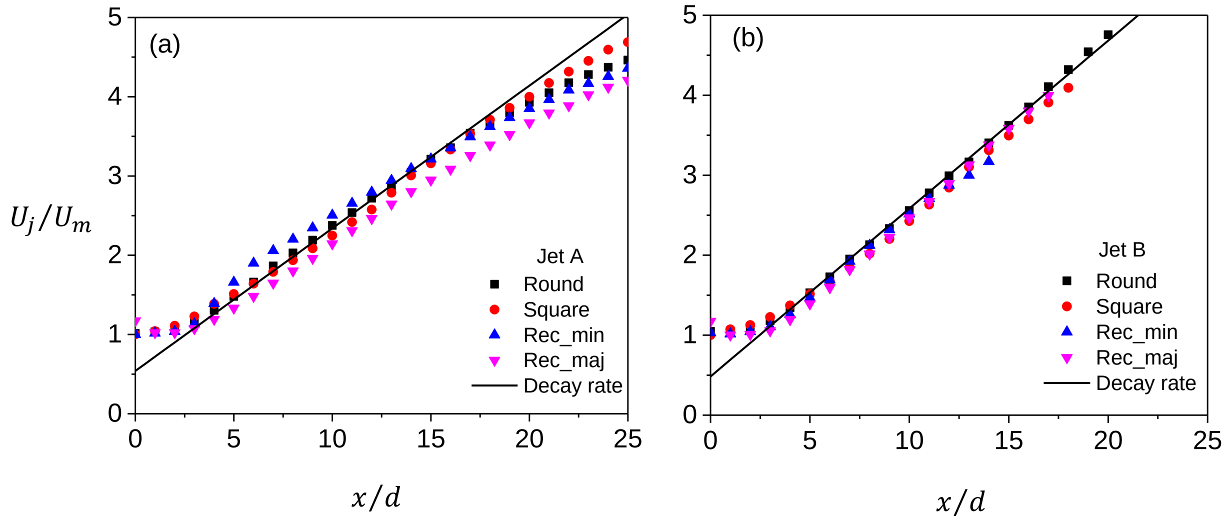

Figure 4. 6 Normalized local streamwise mean velocities (a) Jet A (b) Jet B

Table 4. 3 Decay rate summary for the various nozzle geometries

Geometry	**Jet A**		**Jet B**	
	$K_{d,A}$	**Range** (x/d)	$K_{d,B}$	**Range** (x/d)
Round	0.18	$3 \le x/d \le 15$	0.21	$3 \le x/d \le 20$
	0.12	$15 \le x/d \le 25$		
Square	0.18	$2 \le x/d \le 25$	0.20	$4 \le x/d \le 18$
Rect_minor	0.20	$3 \le x/d \le 10$	0.20	$3 \le x/d \le 14$
	0.12	$12 \le x/d \le 25$		
Rect_major	0.17	$3 \le x/d \le 18$	0.20	$3 \le x/d \le 17$

From Jet A in Table 4.3, the round and rect_min jets show two different decay rates within the measurement domain. Further downstream from the jet exit, $x/d \geq 12$, the round and rect_min jets showed a 33% and 40% reduced decay rates, respectively, when compared to the decay rates within $3 \leq x/d \leq 12$. Within the early interaction region of Jet A, the rect_min jet shows an 11% higher decay rate compared to the round and square jets, and an 18% higher rate when the nozzle is re-oriented to the major plane. This is consistent with the rapid expansion of the jet produced from rect_min nozzle and its enhanced mixing capability.

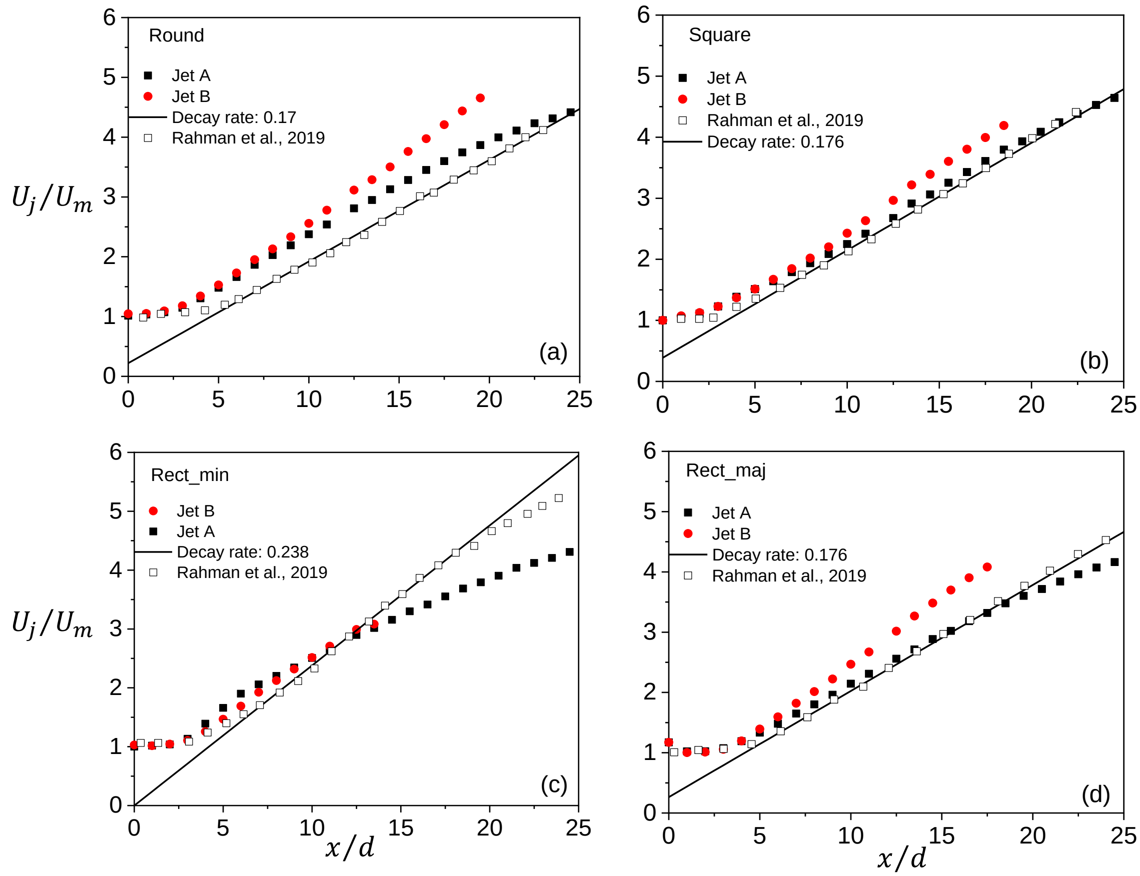

Figure 4. 7 Normalized local streamwise mean velocities (a) Round (b) Square (c) Rect_minor (d) Rect_major

From Fig. 4.6b, irrespective of nozzle geometry, Jet B decays at comparable rates. Compared to

Jet A, a faster decay rate is evident for all geometries except rect_min (see Table 4.3). This is because of the available ambient fluid for entrainment in Jet B relative to Jet A. In the case of rect_min, both jets exhibit comparable decay rates. The present submerged twin jets are compared to the submerged single jet results from Rahman et al. (2019) in Fig. 4.7. The decay rates of the submerged single jets are shown on the plots. Considering the round jet (Fig. 4.7a), the submerged single jet is characterized by a single decay rate that decays at a comparable rate with Jet A within $3 \leq x/d \leq 15$ but at a 19% reduced decay rate when compared to Jet B. For the square and major oriented rectangular jets (Fig. 4.7b and d), the submerged single jet decayed at comparable rates to Jet A but at a 12% reduced rate when compared to Jet B. The submerged single rect_min jet (Fig. 4.7c) shows a reduction in decay rate in the far-field ($x/d \geq 18$), similar to what is observed in the submerged twin jet. However, the decay rates in the submerged single jet were generally higher than in both Jets A and B of the twin jets. Rahman et al. (2019) attributed the reduction in decay rate in the far-field to the reduced entrainment.

As noted in Chapter 1, a submerged jet is characterized by the deviation of the location of the local maximum velocity towards the free surface (Madnia and Bernal 1994; Tay et al., 2017a). To examine this behaviour, a plot of the loci of the local maximum velocity, y_m is presented in Fig. 4.8 for both jets A and B. The rates of deflection of Jet A are estimated using a least-square linear fit as shown in Fig. 4.8a and the results are presented in Table 4.4.

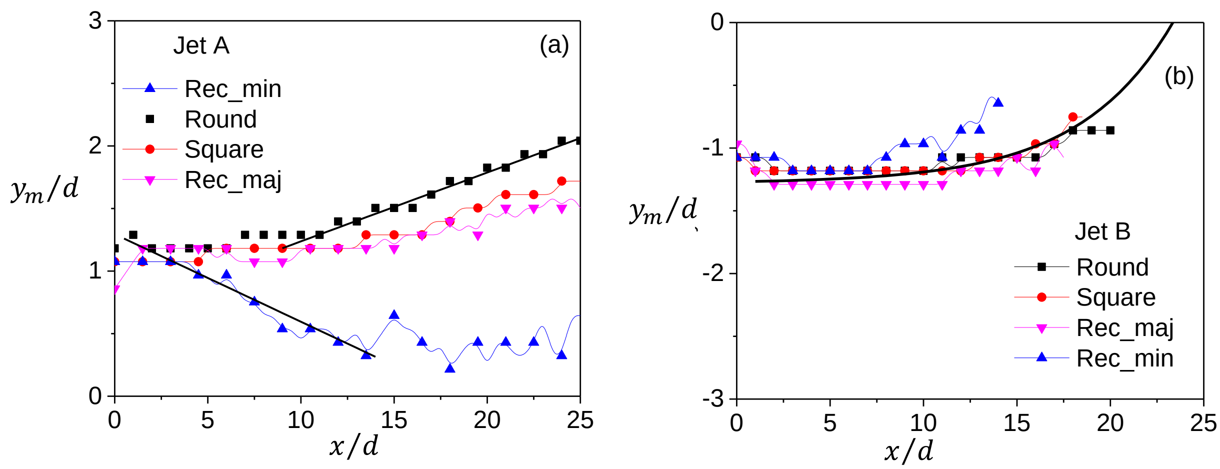

Figure 4. 8 Distribution of the locations of the maximum mean velocity of (a) Jet A measured from the free surface (b) Jet B measured from the center plane $(y/d = 0)$

Table 4. 4 Deflection of the location of the local maximum velocity of jet A

Geometry	Deflection rate	Range
Round	0.055	$10 \leq x/d \leq 25$
Square	0.040	$12 \leq x/d \leq 25$
Rect_min	0.070	$4 \leq x/d \leq 13.5$
Rect_maj	0.030	$13.5 \leq x/d \leq 25$

From Fig. 4.8a, the deflections occur after the merging point for all geometries. In agreement with the literature, deflection towards the free surface is observed in Jet A, for the jets issuing from round, square and rect_maj nozzles. Contrary to this, jet issuing from rect_min nozzle shows a deflection towards the center plane between jets A and B and this deflection occurred prior to the jet's attachment to the free surface. Compared to the rec_min jet which shows the largest deflection rate in Jet A, the round, square and rect_maj jets showed reduced deflection rates of 21%, 43%

and 57%, respectively. The onset of the deflection of the round, square and rect_maj jets towards the free surface occurred in the order of the earliest attachment to the free surface. The deflection rates in the submerged single jet of Rahman et al. (2019) are 51% and 33% lower than the present round and square jets but 43% and 33% higher than the present rect_min and rect_maj jets.

Figure 4.8b shows the deflection in Jet B. With the exception of the rect_min jet, all other jets followed an exponential growth given by equation (4.5) and the jets approach the center plane at about $x/d = 23$.

$$y_m^B/d = -1.28 + 0.012exp(0.2\,x/d) \tag{4.5}$$

4.2.3 Half-velocity width

To study the spreading of the outer shear layer of jet B, profiles of the half-velocity width are shown in Fig. 4.9. To quantify the spread rate, equation (1.3) is used and the least-squares straight line is as shown in the figures. The results of the spread rates for the geometries studied are reported in Table 4.5. The jets began spreading after the potential core but a further delay in the onset of spreading occurred in the rect_maj jet. This is because of the axis-switching phenomenon as previously explained. Hussain and Husain (1989) identified the location of axis-switching as the point where the half-velocity widths of the rect_min and rect_maj equate each other. The dotted vertical line in Fig. 4.9a shows this point of intersection to occur at $x/d = 3$. This result is 20% higher than the axis-switching location reported by Rahman et al. (2019) in the single submerged jet but falls within $x/d = 1$ to 3.5 reported in previous asymmetric nozzle (elliptic and rectangular) studies of (Hussain and Husain 1989; Aleyasin et al., 2017a). Downstream of $x/d = 5$, the rect_maj jet begins to spread at a 10% lower rate to the rect_min jet. The rect_min jet shows the greatest spread rate that exceeds the spread rates of the round and square jets by about 33%.

The outer shear layer of Jet B spreads at a comparable rate to the outer shear layer of the single submerged jet of Rahman et al. (2019), irrespective of nozzle geometry. This suggests that the presence of Jet A and its interaction with Jet B has no substantial effect on the spread rate of the outer shear layer of Jet B. Similarly, comparing the spread rate in the outer shear layer of the present submerged twin round jets study to the free twin round jets study of Aleyasin and Tachie (2019) reveals a 17% higher spread rate in the twin free jets. This discrepancy could be attributed to the difference in nozzle geometry and nozzle separation ratio as Rahman and Tachie (2018) reported negligible confinement effect on the development of the outer shear layer of Jet B.

To obtain a reliable comparison of symmetric and asymmetric jets, an equivalent half-velocity width of the major and minor rectangular nozzle jets is used in free jet studies to provide an average spreading rate of the rectangular nozzle. Following Aleyasin et al., (2017a) and Hussain and Husain (1989), the average spread rate was obtained from equation (4.6). The result gives an intermediate value between the results of the major and minor orientations as shown in Table 4.5.

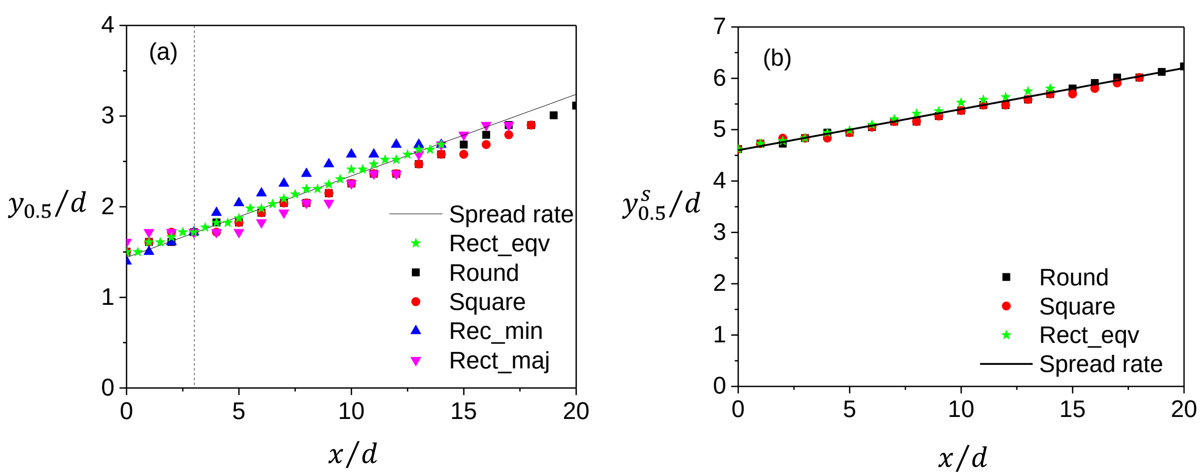

Figure 4. 9 Half velocity width in the outer shear layer of jet B measured from (a) the location of local maximum velocity (b) the free surface

Table 4. 5 Spread rates in the outer shear layer of jet B

Geometry	**Spread rates (k_s)**	**Range**
Round	0.083	$3 \leq x/d \leq 20$
Square	0.083	$3 \leq x/d \leq 20$
Rect_minor	0.110	$4 \leq x/d \leq 10$
Rect_major	0.100	$5 \leq x/d \leq 12$
Rect_equivalent	0.105	$4 \leq x/d \leq 11$

$$(y_{0.5})_{\mathrm{eqv}} = \sqrt{(y_{0.5})_{\mathrm{minor}} \times (y_{0.5})_{\mathrm{major}}} \quad (4.6)$$

The average spread rate of the equivalent rectangular jet is 27% higher compared to the round and square jets. This result is consistent with the previously reported enhanced growth rate in a rectangular free jet over round and square free jets (Aleyasin et al., 2017a). With the free surface as a reference, the spreading in the outer shear layer of jet B is shown in Fig. 4.9b. The result shows a spread rate of 0.080, irrespective of nozzle geometry and in close agreement with the spread rate of 0.078 reported in the submerged single round jet study of Madnia and Bernal (1994).

4.2.4 Surface-normal profiles

Figure 4.10 shows one-dimensional profiles of the mean velocity, turbulence intensity and Reynolds shear stress at selected streamwise locations. The length and velocity scales used to normalize the profiles are the nozzle diameter (d) and local maximum velocity (U_m) of jet A. The nozzle diameter, d, is chosen as a length scale so that the vertical extent is terminated at the free surface, which is located at $y/d = 3.1$, as in all other plots. The choice of offset height, h, as a length scale has no effect on the profiles. The selected locations, $x/d = 2, 6, 10$ and 18, span the converging and merging regions. Downstream of $x/d = 2$, the highest spread rate of the rect_min jet results in increasing U/U_m, with rect_maj showing the least velocity. Further downstream ($x/d = 18$), the rect_maj recovers and shows comparable center plane velocity to the round and square jets. At $x/d = 6$, the rect_min shows a decreased peak velocity of jet A (within the shear layer) owing to its enhanced decay rate within $4 \leq x/d \leq 7$ as shown in Fig. 4.6a.

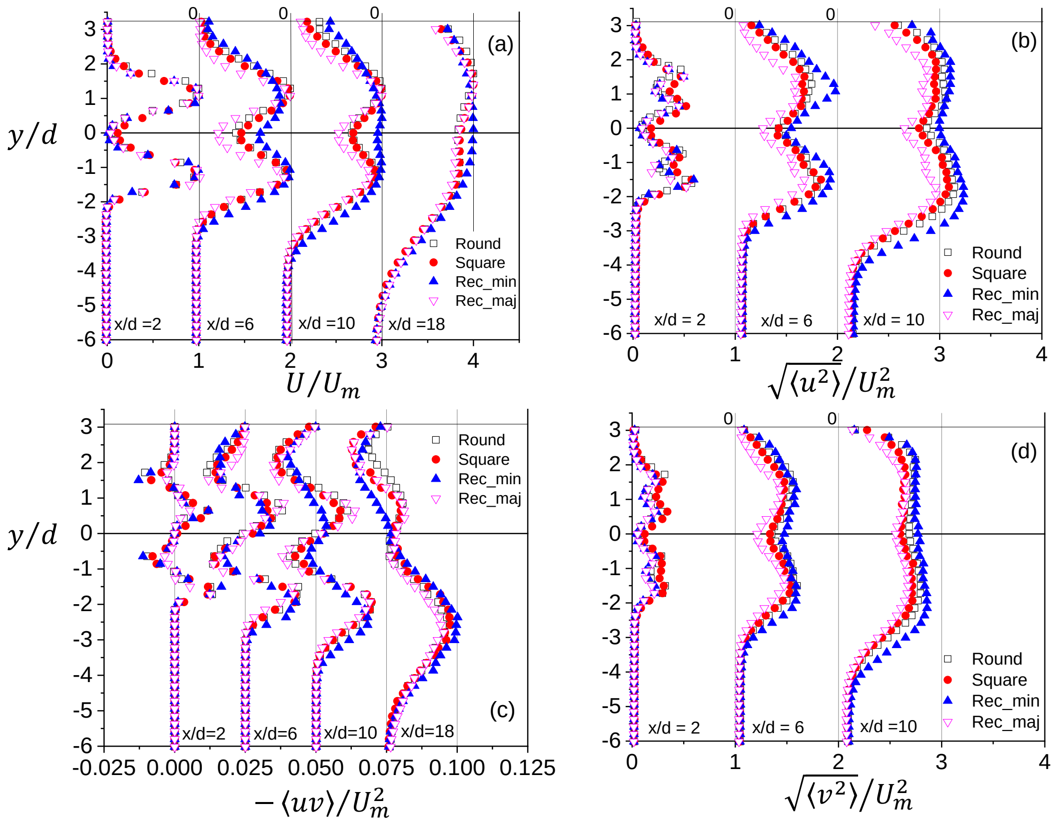

Figure 4. 10   Streamwise profiles of (a) mean velocities (b) streamwise turbulence intensity (c) Reynolds shear stress (d) surface normal turbulence intensity

At $x/d = 6$ and 10, the rect_min jet shows enhanced velocity at the free surface compared to all other jets. This is consistent with the characteristic non-zero velocity of surface jet and the enhancement in the rect_min jet is due to its earlier attachment to the free surface. This difference in the profiles become negligible as the rect_min jet combines at $x/d = 18$.

Figure 4.10b shows the profiles of the streamwise turbulence intensity. All geometries show comparable values at $x/d = 2$ with peak intensities occurring within the shear layers of each jet. As the jet evolves downstream, the double peaks in each of the upper and lower shear layer of Jets A and B vanish as turbulence intensity increases along the nozzle centerline. A plot of the turbulence intensity against streamwise distance (not shown) revealed turbulence intensity peaks at $x/d = 3.5 \pm 0.5$, irrespective of nozzle geometry. As the jets interact in the merging region at $x/d = 6$, the rect_min jet shows higher values of $\sqrt{\langle u^2 \rangle}/U_m$ within the shear layers and at the nozzle centreline compared to the other jets. Along the nozzle centrelines, the rect_min jet shows 37% and 27% higher levels of streamwise turbulence intensity compared to the round jet for Jets A and B, respectively. Comparing the profiles of the streamwise (Fig. 4.10b) and surface-normal (Fig. 4.10d) turbulence intensities, it is evident that surface-normal values show lower peak values compared to the streamwise values. For example, the centreline streamwise turbulence intensity of Jet A at $x/d = 6$ for the rect_min jet is 24% higher than the surface-normal turbulence intensity. This is consistent with the large-scale anisotropy previously reported in submerged jet studies (Anthony and Willmarth 1992; Walker et al, 1995; Tay et al, 2017a). At $x/d = 10$, all jets are in the surface jet region and show no significant difference in peak values of $\sqrt{\langle u^2 \rangle}/U_m$ and $\sqrt{\langle v^2 \rangle}/U_m$ between Jet A and Jet B. The effect of nozzle geometry on the Reynolds shear stress is shown in Fig. 4.10c. Negative and positive peak values occur in the upper and lower shear layers of each jet. As the rect_min jet combines to form a single jet at $x/d = 18$, it is characterized by a single negative and positive peak values above and below the center plane respectively.

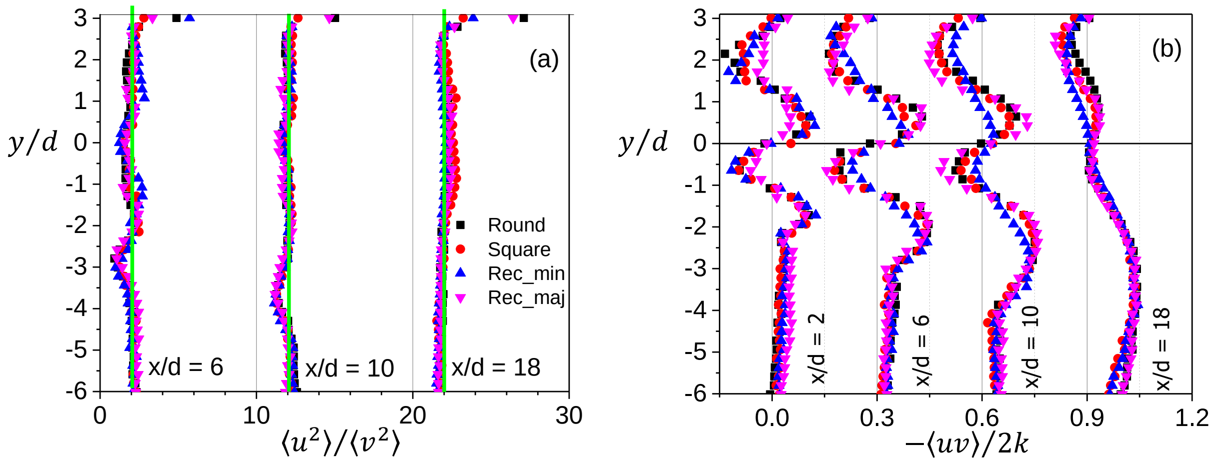

Figure 4. 11 Surface-normal profiles of Reynolds stress ratios (a) Reynolds normal stress ratio (b) Townsend structure parameter

The presence of the free surface suppresses peak values of $-< uv >/U_m^2$ in Jet A relative to Jet B. For instance, at $x/d = 10$ and 18, the magnitude of the peak Reynolds shear stress in the outer shear layer of Jet A is 43% and 40%, respectively, lower than in the outer shear layer of Jet B. These degrees of suppression by the free surface is independent of nozzle geometry.

To explore the anisotropy alluded to in Fig. 4.10, profiles of Reynolds stress ratios are presented in Fig. 4.11. Result of the Reynolds normal stress ratio (Fig. 4.11a) shows that within the interaction region, irrespective of nozzle geometry, $\langle u^2\rangle/\langle v^2\rangle \approx 2$ as shown by the green solid line. As the free surface is approached, $\langle u^2\rangle/\langle v^2\rangle \approx 5$. This increased anisotropy at the free surface further increases downstream to $\langle u^2\rangle/\langle v^2\rangle \approx 7$ at $x/d = 18$. Consistent with previous submerged jet studies (Essel and Tachie, 2018; Rahman et al., 2019; Tay et al., 2017), these observations suggest that standard two-equation models such as the $k - \varepsilon$ model where isotropic turbulence assumption ($\langle u^2\rangle/\langle v^2\rangle \approx 1$) is implied will not be able to accurately predict the mean properties of this flow. Rather, models that directly solve the Reynolds stresses would be more appropriate.

Profiles of the Townsend structure parameter, $a_1 = -\langle uv \rangle / 2k$ (where k is the turbulent kinetic energy) are shown in Fig. 4.11b. This parameter, associated with the model coefficient, $C_\mu = (-\langle uv \rangle / k)^2$ in standard eddy viscosity models, is generally assumed a constant ($a_1 = 0.15$) and result in $C_\mu = 0.09$. It is obvious from Fig. 4.11b that a_1 is not a constant and varies with nozzle geometry, and also across the jets and with downstream distance. Along the center plane ($y/d = 0$), nozzle centreline and free surface, this parameter goes to zero within $2 \leq x/d \leq 10$. At $x/d = 18$, the peak values are less than 0.15 as the free surface is approached.

4.3 Streamwise Evolution of Surface Velocity, Turbulence Intensity, and Vorticity Thickness

4.3.1 Streamwise evolution of surface mean velocity and velocity defect

Figure 4.12a shows the downstream evolution of the free surface velocity for all nozzle geometries studied. Profiles of a submerged single jet issuing from round and rect_min nozzle (Rahman et al., 2019) are included for comparison. To concentrate on the twin jet-free surface interaction, the streamwise distance is measured relative to the attachment points of the jets, i.e., the solid line at $(x - L_a)/d = 0$ represents the attachment point. Following Tay et al. (2017a), the free surface location was obtained from the examination of several plots of the mean streamwise velocity profiles along horizontal lines that are within 10 vector spacings from the upper edge of the field-of-view. The free surface was chosen to be at a surface-normal location where, within measurement uncertainty, there was no significant variation in the profiles above and below. As seen from the plot, the surface velocity is zero prior to the attachment point ($(x - L_a)/d = 0$). Irrespective of nozzle geometry, the mean velocities at the free surface initially increase downstream of the attachment point, albeit at varying rates to peak values followed by a decrease.

The spatial acceleration or rate of increase of the mean velocities with streamwise distance is much higher than the spatial deceleration which occurs downstream of the peaks.

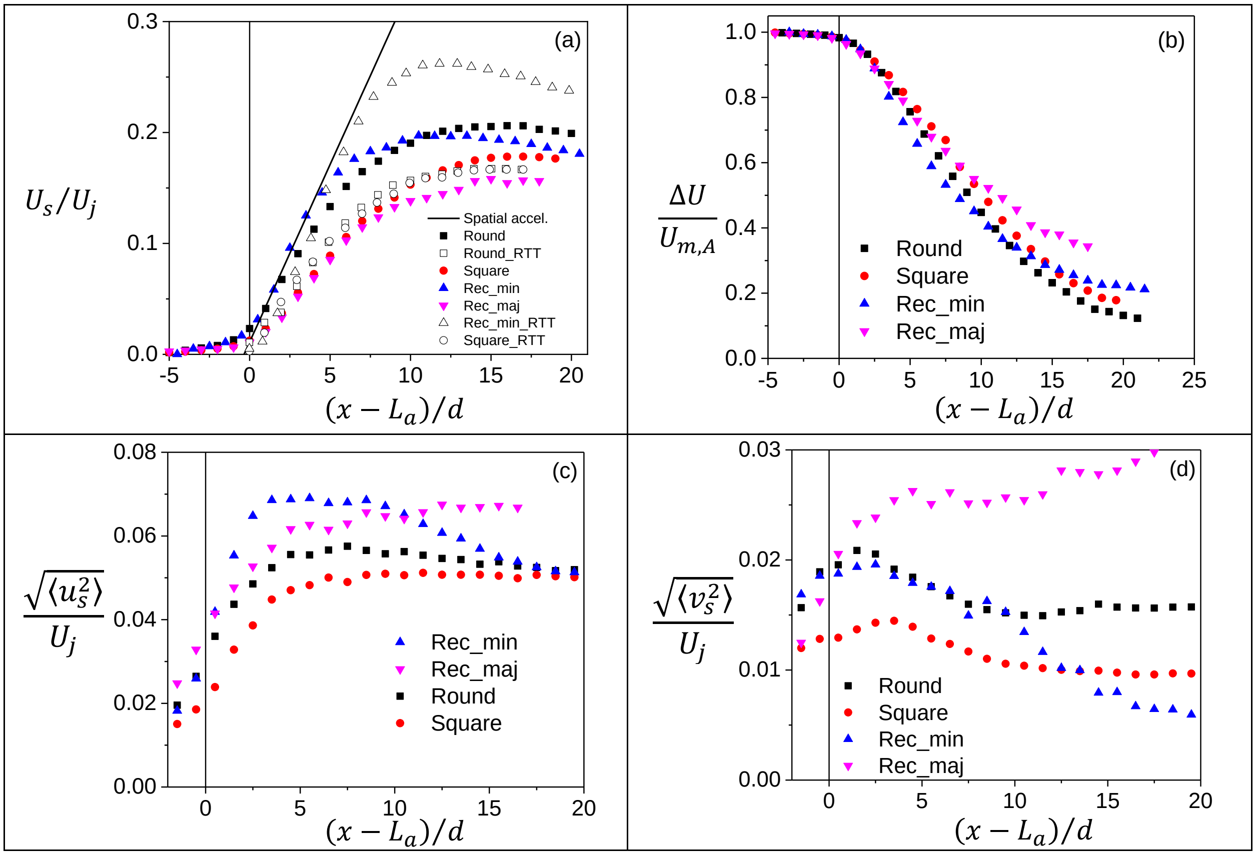

Figure 4. 12 Streamwise evolution of (a) mean surface velocity (b) mean velocity defect (c) streamwise turbulence intensity (d) surface-normal turbulence intensity. RTT = Rahman et al., 2019

A similar trend is reported by Essel and Tachie (2018), Madnia and Bernal (1994) and Tay et al. (2017a) and the free surface is said to be in a state of strain resulting from the alternating acceleration and deceleration. To estimate the spatial acceleration of the mean velocities along the free surface, a least-squares line was fitted to the data downstream of the attachment point and the slope of the line estimated the acceleration of the surface mean velocities. From Fig. 4.12a, the rect_min jets accelerated the surface mean velocity at a 39% faster rate when compared to the round jets while the acceleration by the square and rect_maj jets occurred at comparable rates. The rect_min jets accelerated the mean surface velocity to a peak value that is 30% lower than observed in the submerged single jet. The reason for this is due to the stronger attraction between the rect_min jets that result in the deviation of the location of the local maximum velocity (y_m) of Jet A away from the free surface as seen in Fig. 4.8a. Considering the single and twin submerged jets issuing from the round nozzle, the mean surface velocity attained a peak value in the twin jets that is 24% higher than in the single jet. Profiles of the mean surface velocity defect, $\Delta U = \left(U_{m,A} - U_s\right)$, normalized by the local maximum streamwise velocity of Jet A are shown in Fig. 4.12b as a function of $(x - L_a)/d$. Consistent with the study of Tay et al. (2017a), the results show an exponential decay with downstream distance and a good collapse of the profiles within $0 \leq (x - L_a)/d \leq 5$. Downstream of $(x - L_a)/d = 10$, the mean surface velocity defect in the twin round and square jets decreases beyond the rect_min twin jets.

4.3.2 Streamwise evolution of turbulence intensities along the free surface

Profiles of the streamwise and surface-normal turbulence intensities along the free surface are shown in Fig. 4.12c and 4.12d, respectively. The turbulence intensities are normalized by the jet exit velocity. The rates of increase and decrease of the turbulence intensities are estimated from the slope of the least-squares line fitted to the data. Downstream of the attachment point within $0 \leq (x - L_a)/d \leq 3$, the surface streamwise turbulence intensities increased at comparable rates for the round, square and rect_maj jets. The rect_min jet increased at an 86% higher rate over all other jets due to its earlier interaction with the free surface. Downstream of $(x - L_a)/d = 3$, the growth rates reduced by 89%, 71% and 93% for the round, square and rect_maj jets, respectively, while the rec_min jet maintained a constant peak value of 0.069 within $4 \leq (x - L_a)/d \leq 8$. A decrease of the surface streamwise turbulence intensity is observed for the round and rect_min jets downstream of $(x - L_a)/d > 8$. At this downstream distance, the square and rect_maj jets show a constant peak value and an increasing $\sqrt{\langle u_s^2 \rangle}/U_j$, respectively. The region of decreasing $\sqrt{\langle u_s^2 \rangle}/U_j$ is absent in the case of the square and rect_maj jets within the measurement window due to their late interaction with the free surface. This delayed jet-free surface interaction explains the constant peak and acceleration observed in the square and rect_maj jets downstream of $(x - L_a)/d = 8$, respectively.

Downstream of $(x - L_a)/d = 2$ in Fig. 4.12d, surface-normal turbulence intensity at the free surface decreased for the round, square and rect_min jets, with the exception of the rect_maj jet due to the delay in the onset of its jet-free surface interaction. The rate of decrease in the square and rect_min jets reduced by 13% and 25%, respectively when compared to the round jet. An examination of Fig. 4.12c and d reveals that as $\sqrt{\langle v_s^2 \rangle}/U_j$ decreases downstream of $(x - L_a)/d = 2$, $\sqrt{\langle u_s^2 \rangle}/U_j$ increases and attain peak values that are about three and a half times the peak values of $\sqrt{\langle v_s^2 \rangle}/U_j$, irrespective of nozzle geometry. This is an indication of a strong anisotropy at the free surface resulting from the damping of surface-normal turbulence intensities and is consistent with the redistribution of turbulent kinetic energy at the free surface from the surface-normal component to components parallel to the free surface (Anthony & Willmarth, 1992; Swean et al., 1989; Walker et al., 1995). At $x/d = 18$, corresponding to $(x - L_a)/d = 12.8$ for the round jets, it is evident that the surface-normal profiles of Reynolds normal stress ratio at this location $(\langle u^2 \rangle / \langle v^2 \rangle \approx 7)$, underestimated the anisotropy at the free surface by 43%.

4.3.3 Streamwise evolution of vorticity thickness

To quantify the growth of the outer shear layer of jet A, the vorticity thickness, δ_ω is used (Ashcroft and Zhang, 2005). The vorticity thickness is estimated using equation (4.7) shown below:

$$\delta_\omega = \Delta U / \left(\frac{\partial U}{\partial y}\right)_{max} \tag{4.7}$$

where $\Delta U = U_{m,A} - U_s$, is the surface mean velocity defect and $(\partial U/\partial y)_{max}$ is the local maximum mean shear in the outer shear layer of Jet A. The streamwise evolution of the vorticity thickness for all geometries studied is presented in Fig. 4.13. Within the pre-attachment region, linear growth of the vorticity thickness is observed and the growth and decay rates, estimated as the slope of the least-squares line fitted to the data, are presented in Table 4.6 for all geometries. This near-field growth of the vorticity thickness is consistent with the downstream growth of the vortices generated by the shear instability. From the results, the rect_min jet shows the most rapid growth of the vorticity thickness (consistent with the rapid expansion of its shear layers) while the rect_maj shows the least growth. Comparing these growth rates to those of the submerged single jet of Rahman et al. (2019) shows comparable growth rates for the round, square and rect_maj jets while the present rect_min jet shows an 8% reduced rate.

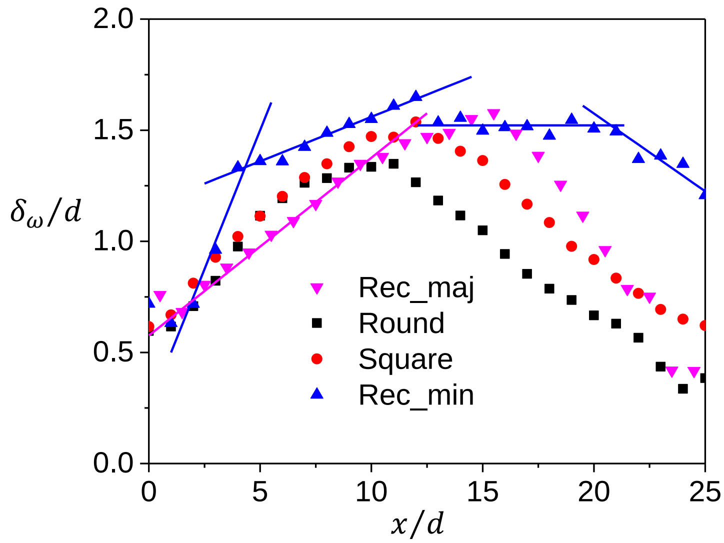

Figure 4. 13 Streamwise evolution of vorticity thickness

The present values for the round, square and rect_min jets fall within the range reported for vorticity thickness in turbulent shear flows such as mixing layers (Brown and Roshko, 1974), separated and reattached shear layers over forward-facing steps (Essel et al. 2015b; Nematollahi and Tachie 2018) and backward-facing step (Essel and Tachie 2015). The result of the rect_min jet shows that within the early interaction region with the free surface ($5 \leq x/d \leq 12$), the free surface reduced the shear layer growth by 84% and subsequently remained constant for about eight nozzle diameters downstream.

Table 4. 6 Growth and decay rates of vorticity thickness

Nozzle Geometries	**Growth Rates**	**Range**	**Decay Rates**	**Range**
Round	0.12	$1 \leq x/d \leq 6$	0.075	$11 \leq x/d \leq 25$
Square	0.10	$0 \leq x/d \leq 7$	0.075	$12 \leq x/d \leq 25$
Rectangular minor	0.25	$1.5 \leq x/d \leq 4.5$	0.070	$21 \leq x/d \leq 25$
Rectangular major	0.08	$1.5 \leq x/d \leq 10.5$	0.135	$16.5 \leq x/d \leq 25$

Beyond this point, ($x/d = 21$), the vorticity thickness decays at a 72% lower rate relative to its growth rate in the pre-attachment region. This downstream decay of the vorticity thickness upon interaction with the free surface suggests the shrinking of the vortices and is consistent with the visualization result of Fig. 4.5c. A similar trend of the vorticity thickness is observed in all other geometries with the exception of the region of constant vorticity thickness. The effect of the free surface leading to the reduction of the growth of the outer shear layer of Jet A occurred within ($4.5 \pm 0.5d$) in the early interaction region for all other jets. The decay of the vorticity thickness commenced subsequently, at an 87% faster rate in the rect_maj jet relative to the rect_min jet and at a 93% faster rate relative to the round and square jets. The slower growth and faster decay rate in the rect_maj jet could be a consequence of the axis-switching phenomenon that resulted in the delayed onset of jet-free surface interaction.

4.4 Two-Point Velocity Auto-correlation

To investigate the effect of the free surface and the interaction between twin jets on large-scale structures, a two-point auto-correlation of streamwise and surface-normal velocity fluctuations is used. As previously mentioned in section 2.2.1, equation (2.1) is used to obtain the correlation function of an arbitrary quantity A between two spatial locations $A(x, y)$ and $A(x + \Delta x, y + \Delta y)$ as follows:

$$R_{AA}\left(x_{ref} + \Delta x, y_{ref} + \Delta y\right) = \frac{\overline{A\left(x_{ref}, y_{ref}\right) A\left(x_{ref} + \Delta x, y_{ref} + \Delta y\right)}}{\sigma_A\left(x_{ref}, y_{ref}\right) \sigma_A\left(x_{ref} + \Delta x, y_{ref} + \Delta y\right)}$$

The two-point auto-correlation analysis is performed in the pre-attachment region ($x/d = 4$) and the surface jet region at ($x/d = 8$ and 16). At these locations, the two-point auto-correlation was performed at surface-normal locations of the local maximum velocities of both jets A and B ($y/d = y_{m,A}\ and\ y_{m,B}$). Also, to examine the effect of the jet-free surface interaction on the large-scale structures, the analysis was performed in the surface jet region at $(x - L_a)/d = 1, 3$ and 10 at a fixed surface-normal location from the free surface ($y_s = 0.5d$). At all the locations, iso-contours of the correlation function are presented for the jets issuing from the round, square, rect_min and rect_maj nozzles.

Figure 4.14 shows the contours of the two-point auto-correlation function of the streamwise velocity fluctuations, R_{uu}, for Jets A and B in the pre-attachment region ($x/d = 4$) and in the surface jet region ($x/d = 8\ and\ 16$). Consistent with the literature, the structures are elongated in the streamwise direction as the jets evolve downstream. In the surface jet region, the structures in Jet B are spatially more coherent compared to Jet A for all geometries except rect_min. This suggests that the presence of the free surface acts to suppress the growth of the structures in Jet A as the location of the local maximum mean velocities in all three geometries deviate towards the free surface while that of rect_min deviates away from the free surface.

To quantify the size of the structures shown in Fig. 4.14, the streamwise extent of R_{uu}, L_{uu}^{x} was estimated following Christensen and Wu (2005) and Volino et al. (2007), as twice the distance from the self-correlation peak to the most downstream point on the $R_{uu} = 0.5$ contour level. Figures 4.15a and b show the result of the downstream evolution of L_{uu}^{x} for Jets A and B respectively.

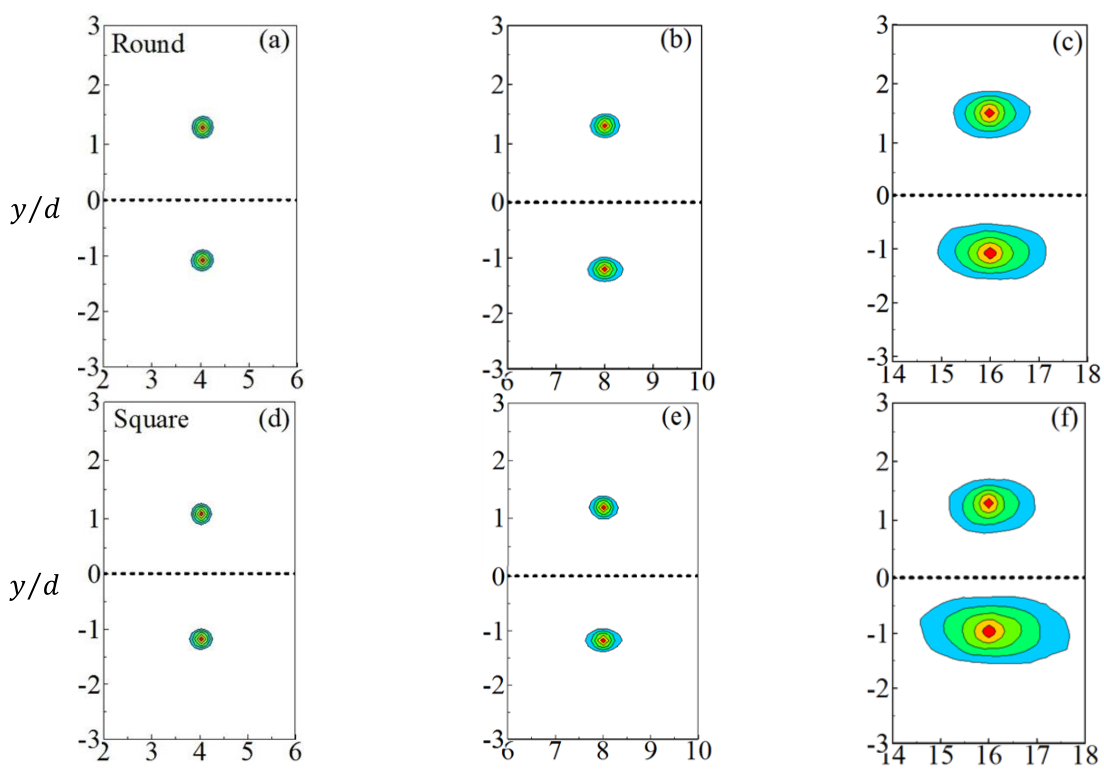

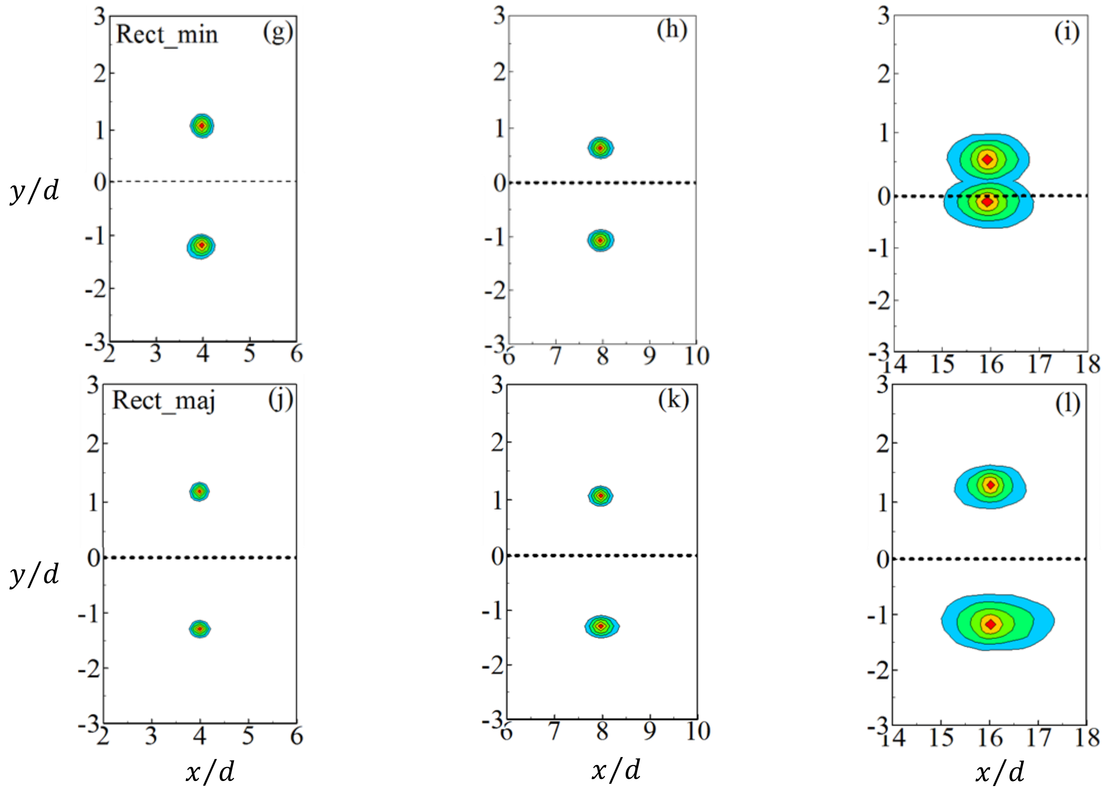

Figure 4. 14 Iso-contours of R_{uu} of twin jets at $y/d = y_m$: Round at $x/d = 4, 8$ and 12 $(a, b$ and c, respectively), Square at $x/d = 4, 8$ and 12 (d, e, and f, respectively), Rect_min at $x/d = 4, 8$ and 12 (g, h and i, respectively), Rect_maj at $x/d = 4, 8$ and 12 (j, k, and l, respectively). Contour levels vary from 0.5 to 0.9 at intervals of 0.1

Results from Fig. 4.15a show comparable structure size in Jet A, irrespective of nozzle geometry within $2 \leq x/d \leq 6$. Downstream of $x/d \geq 8$, the growth rate of the structures is estimated from the slope of the least-squares line fitted to the data. The result shows that the structures grew at comparable rates with the exception of the rect_min jet that grew at a 36% higher rate. Recall that the location of the local maximum velocity in the rect_min jet deviates away from the free surface (see Fig. 4.8a), hence, the reduced suppression effect of the free surface on its structure. The large-scale structures in Jet B were estimated to grow at a rate of 0.16 ± 0.02 irrespective of nozzle geometry.

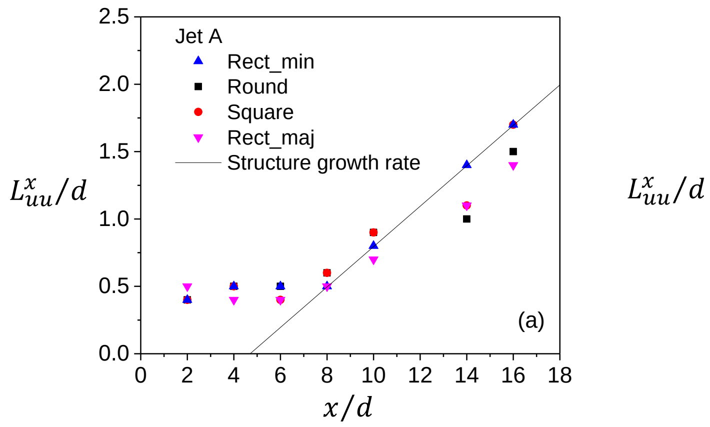

Figure 4. 15 Downstream evolution of the streamwise extent of R_{uu}, L_{uu}^{x}/d in jet A (a) and jet B (b)

Figure 4.16 shows the two-point auto-correlation function of streamwise velocity fluctuations at $(x - L_a)/d = 3, 10,$ and 15 downstream locations from the attachment point and at the surface-normal location of $0.5d$ below the free surface. From the results, the structures grow downstream as observed in Fig. 4.14 and attach to the free surface in the far downstream location of $(x - L_a)/d = 15$. At this downstream location, the structures appear relatively parallel to the free surface. At comparable far-field locations in the submerged single jet of Rahman et al. (2019),

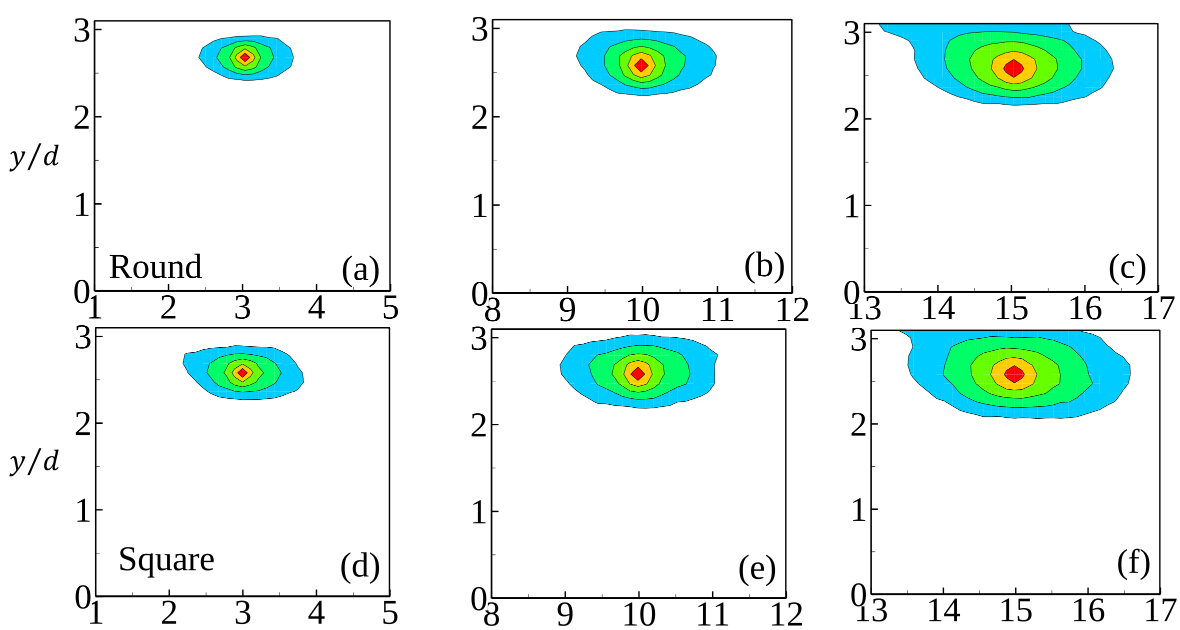

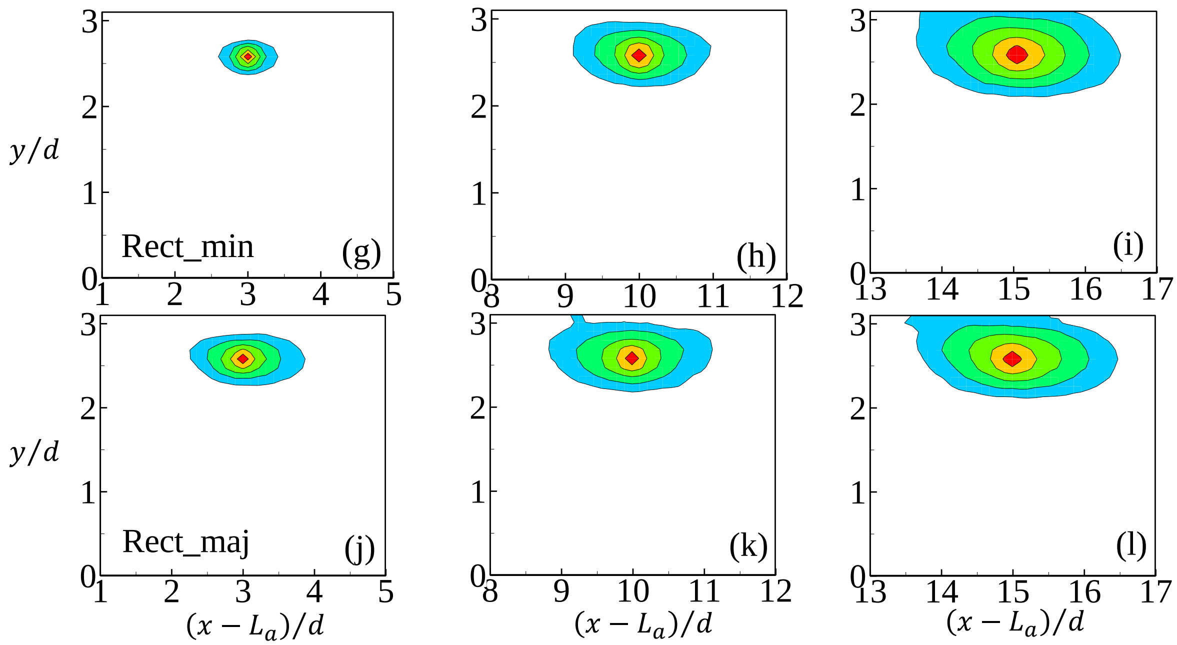

Figure 4. 16 Iso-contours of R_{uu} of twin jets at $y_s/d = 0.5d$: Round at $(x - L_a)/d = 3, 10, \text{and } 15$ $(a, b, \text{and } c)$, Square at $(x - L_a)/d = 3, 10, \text{and } 15$ $(d, e, \text{and } f)$, Rect_min at $(x - L_a)/d = 3, 10, \text{and } 15$ $(g, h, \text{and } i)$, Rect_maj at $(x - L_a)/d = 3, 10, \text{and } 15$ $(j, k, \text{and } l)$. Contour levels vary from 0.5 to 0.9 at intervals of 0.1

similar attachment of the structures to the free surface was reported. However, the structures showed a streamwise inclination angle of about 12 degrees, which decreased as the location of interest moves away from the free surface. A plausible explanation for the absence of structure inclination in the present study is that the presence of Jet B acts to resists the inclination of the structures towards the free surface at this location. A comparison between the streamwise extent of R_{uu}, L_{uu}^{x} of structures close to the free surface ($y_s/d = 0.5d$) and at corresponding Jet A centreline location ($y/d = y_m$), reveals larger structures close to the free surface. However, comparison of the downstream structure sizes from $(x - L_a)/d = 3$ to 15 at $y_s/d = 0.5d$ and $(y/d = y_m)$ shows that the free surface acts to reduce the streamwise growth of the structures.

Figure 4.17 shows the two-point auto-correlation function of the surface-normal velocity fluctuations, R_{vv}, at $y_s/d = 0.5d$ and $(x - L_a)/d = 3, 10$ and 15. The locations correspond to the early, mid and far-field interaction regions of the round, square and rect_maj jets with the free surface. For the rect_min jet, $(x - L_a)/d = 15$ is located in the combined region. Similar to the streamwise extent of R_{uu}, the transverse extent of the two-point auto-correlation function of the surface-normal velocity fluctuations, R_{vv}, L_{vv}^{y} was estimated as the surface-normal distance between the extreme points on the $R_{vv} = 0.5$ contour level. Close to the free surface $(y_s/d = 0.5d)$ and between $(x - L_a)/d = 3$ and 15, L_{vv}^{y} values of the round, square, rect_min and rect_maj jets increased by $75\%, 100\%, 125\%$ and 60% respectively. Contrary to increasing L_{uu}^{x} value as the free surface is approached, L_{vv}^{y} values decrease closer to the free surface when compared to its value at the jet centreline. For instance, at $(x - L_a)/d = 15$ and $y_s/d = 0.5d$, L_{vv}^{y} values for round, square, rect_min and rect_maj jets are 0.7, 0.8, 0.9 and 0.8 respectively. This represents a

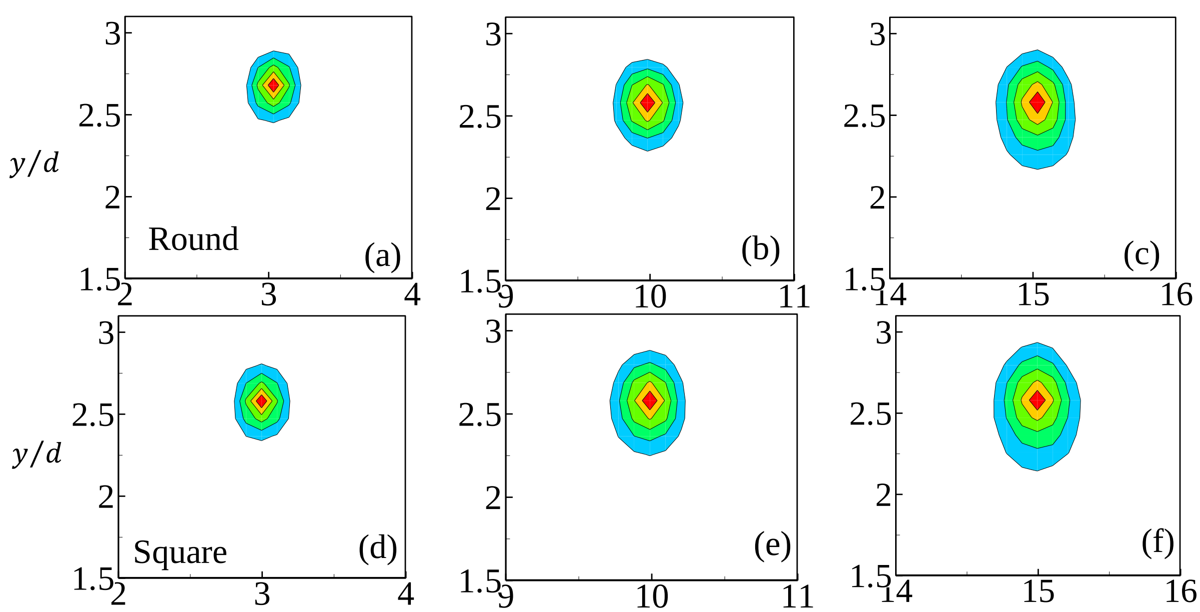

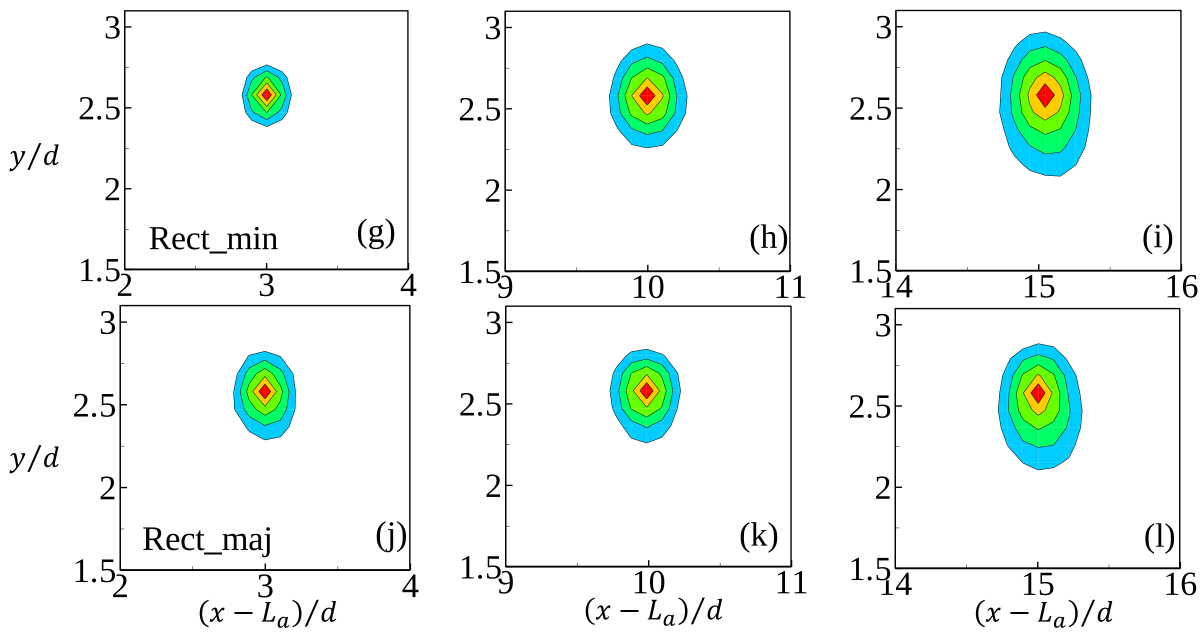

Figure 4. 17 Iso-contours of R_{vv} of twin jets at $y_s/d = 0.5d$: Round at $(x - L_a)/d = 3, 10$ and 15 $(a, b,$ and $c)$, Square at $(x - L_a)/d = 3, 10,$ and 15 $(d, e,$ and $f)$, Rect_min at $(x - L_a)/d = 3, 10,$ and 15 $(g, h,$ and $i)$, Rect_maj at $(x - L_a)/d = 3, 10,$ and 15 $(j, k,$ and $l)$. Contour levels vary from 0.5 to 0.9 at intervals of 0.1

30%, 11%, 10% and 20% reduced surface-normal extent for the round, square, rect_min and rect_maj structures respectively. These results show that the free surface acts to suppress the surface-normal extent of R_{vv} while enhancing its streamwise extent of R_{uu}. This is consistent with the turbulent kinetic energy redistribution at the free surface (see section 4.3.2). Similar observations of the free surface effect on the large-scale turbulent structures are reported in submerged single jets (Tay et al., 2017b; Rahman et al., 2019).

4.5 Joint Probability Density Function (JPDF)

Joint probability density function, $P(u, v)$ is used in this study to investigate the effect of nozzle geometry on turbulent events that contribute to the production of Reynolds shear stress. It is applied at the locations of the local maximum velocity of Jet A, $y_{m,A}$ and at downstream distances of $(x - L_a)/d = -2, +2$ and $+ 4$, spanning the pre-attachment and surface jet regions (Fig 4.18). Following Wallace and Brodkey (1977) and Tay et al. (2017a), JPDF is defined by equation (2.2) and was estimated by sorting the velocity fluctuations into bins of equal width 100×100. As shown in Fig 4.18a, the abscissa and ordinate divide the plot into four quadrants: Q1, Q2, Q3 and Q4, where Q1 $(+u, -v)$ represents fast entrainment of ambient fluid; Q2 $(-u, -v)$ represents slow entrainment of ambient fluid; Q3 $(-u, +v)$ represents slow ejection and Q4 $(+u, +v)$ represents fast ejection. The innermost contours correspond to high-probability, but low-amplitude velocity while the outermost contours correspond to large-amplitude velocity fluctuations (Rahman, 2019). From the results shown in Fig. 4.18, it is evident that at the y_m locations, the JPDF contours are elliptical in shape with no preferred inclination towards any event (because there is no shear at this location as seen in Fig. 4.10c). The shift of the innermost contours towards the positive streamwise fluctuation suggests the dominance of the fast u fluctuations in the Reynolds shear stress production. The Reynolds shear stress producing events become increasingly important as the jets evolve downstream into the merging/interaction region. This is revealed by the streamwise growth of the probability contours, which is more evident in the round and rect_min geometries as their pre-attachment location, $(x - L_a)/d = -2$ correspond to $x/d =$ 2.6 and 3.2 respectively.

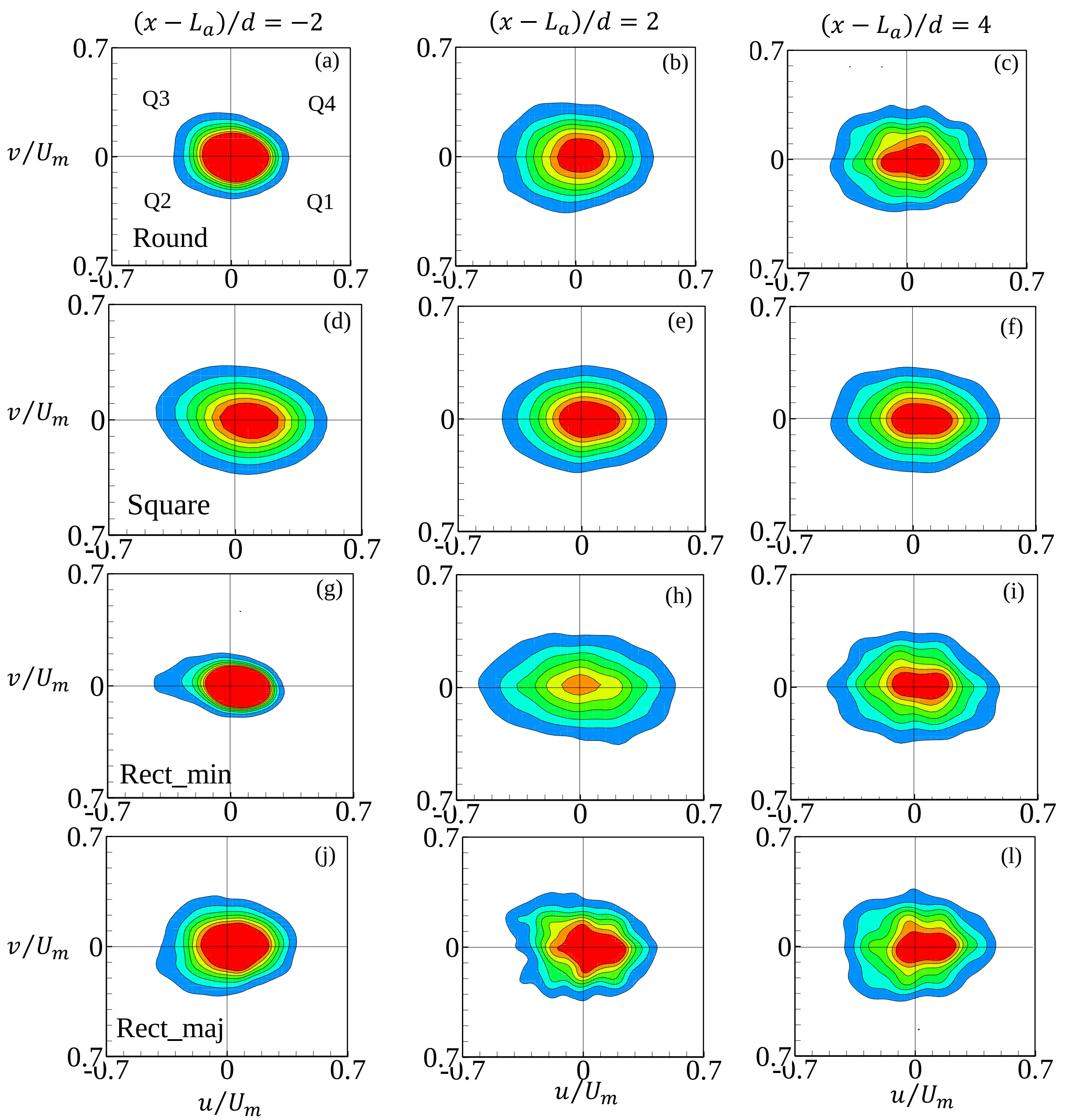

Figure 4. 18 Iso-contours of JPDF at $y/d = y_m$ and varying streamwise locations based on the attachment point. Round jet at (a) $(x - L_a)/d = -2$ (b) $(x - L_a)/d = 2$ (c) $(x - L_a)/d = 4$. Square jet at (d) $(x - L_a)/d = -2$ (e) $(x - L_a)/d = 2$ (f) $(x - L_a)/d = 4$. Rect_min jet at (g) $(x - L_a)/d = -2$ (h) $(x - L_a)/d = 2$ (i) $(x - L_a)/d = 4$. Rect_maj jet at (j) $(x - L_a)/d = -2$ (k) $(x - L_a)/d = 2$ (l) $(x - L_a)/d = 4$. Contour levels are from 0.5 to 3.5 at 0.5 intervals

Figure 4.19 is presented to investigate the turbulent events contributing to the production of Reynolds shear stress within the outer shear layer of Jet A, and to examine the effect of the free surface on the events. The JPDF plots are obtained at two nozzle diameters from the attachment point, $(x - L_a)/d = 2$ and at varying surface-normal locations above the location of the local maximum velocity, $y'/d = +0.5, +1$ and $+\ 1.5$ where y' is the surface-normal distance relative to y_m. The results show that within the shear layer, the JPDF contours are inclined towards the Q2 and Q4 quadrant suggesting that slow entrainment and fast ejection events dominate the contribution to Reynolds shear stress production. As the free surface is approached, a diminishing effect on the JPDF is observed. This trend is consistent with the decay of Reynolds shear stress towards the free surface as shown by the Reynolds shear stress profiles in Fig 4.10c. The damping effect of the free surface is least on the rect_min jet because while the y_m of all other geometries deviated towards the free surface, y_m of rect_min deviated away from the free surface, giving rise to the most separation distance from the free surface.

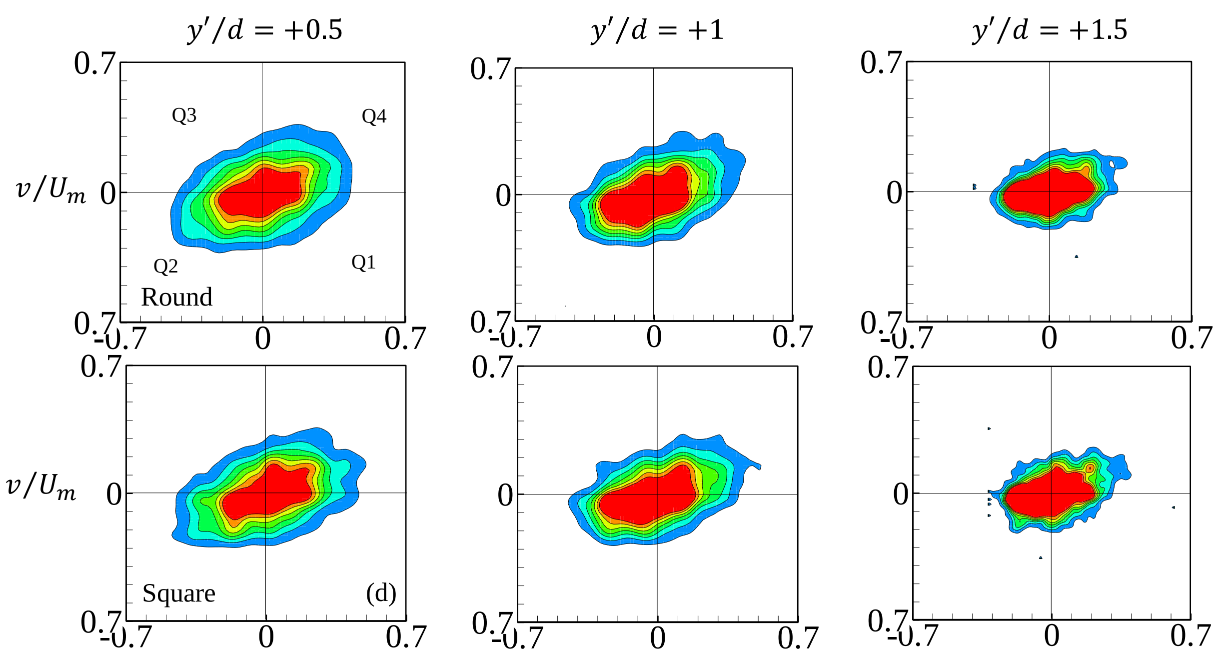

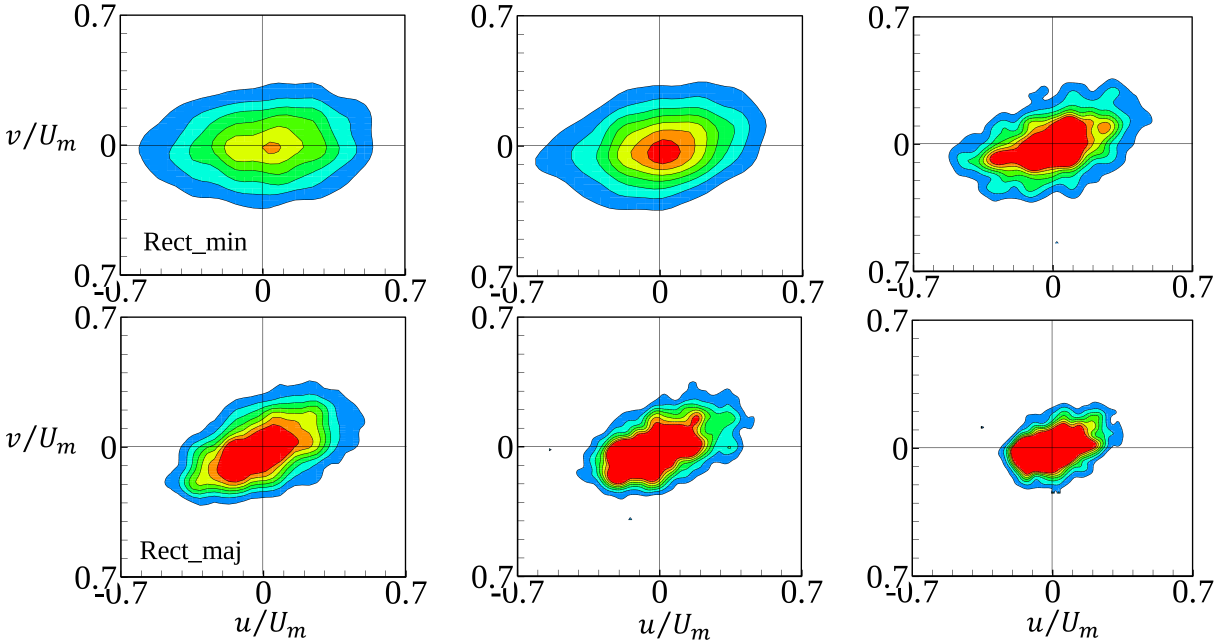

Figure 4.19 Iso-contour of JPDF at $(x - L_a) / d = 2$ and varying surface-normal locations relative to y_m. Round jet at (a) $y' / d = +0.5$ (b) $y' / d = +1$ (c) $y' / d = +1.5$. Square jet at (d) $y' / d = +0.5$ (e) $y' / d = +1$ (f) $y' / d = +1.5$. Rect_min jet at (g) $y' / d = +0.5$ (h) $y' / d = +1$ (i) $y' / d = +1.5$. Rect_maj jet at (j) $y' / d = +0.5$ (k) $y' / d = +1$ (l) $y' / d = +1.5$. Contour levels are from 0.5 to 3.5 at 0.5 intervals

CHAPTER FIVE

CONCLUSION AND RECOMMENDATION

5.1 Conclusion

In this study, an experimental investigation of nozzle geometry effect on the mean and turbulent characteristics and turbulent structure of submerged twin jets was conducted using a planar PIV. The experiments were performed on three different nozzles: round, square, and rectangular (minor and major orientations) geometries at a fixed Reynolds number and offset height of $R_e = 4{,}400$ and $h = 2d$ respectively. The major conclusions from the study are stated as follows:

- The rect_min and square jets showed a 23% reduced potential core length compared to the round and rect_maj jets. The rect_min geometry showed relatively enhanced near field mixing as its faster shear layer expansion resulted in the shortest attachment length to the free surface. Re-orienting the rectangular nozzle from the minor to the major plane results in a 34% increase in attachment length.
- The lower jet, Jet B, decayed at comparable rate, irrespective of nozzle geometry, and was higher than the decay rate in the upper jet, Jet A. For Jet A, the rect_min jet decayed at an 11% higher rate compared to the round and square jets, and at an 18% higher rate over the rect_maj jet.
- The deflection of the location of local maximum velocity, y_m in Jet A is dependent on nozzle geometry. The y_m of round, square and rect_maj deflected towards the free surface

while that of rect_min deflected away from the free surface. Compared to the rect_min jet, the round, square and rect_maj jets deflected at lower rates of 21%, 43% and 57%, respectively.

- The Reynolds stress ratio at the free surface is 60% higher than within the flow and grows by 40% at the free surface as the flow propagates downstream from $x/d = 6$ to 18. Surface-normal profiles of the turbulent statistics show that isotropic assumption is not applicable to this flow, irrespective of nozzle geometry.
- Rect_min jets increase the mean surface velocity at a 39% higher rate over the round jets while the square and rect_maj jets show comparable rates that are lower than the round jet. A strong anisotropy at the free surface resulting from the damping of surface-normal turbulence intensities is evident in the round, square and rect_min jets.
- In the near-field region, the growth rate of the vorticity thickness in the round and square jets is approximately 56% lower than observed in the rect_min jet, and is consistent with the larger shear layer expansion of the rect_min jet. Re-orienting the rectangular nozzle from the minor to the major plane decreases the growth rate by 68%.
- Two-point auto-correlation function shows that turbulent structures elongated in the streamwise direction in all jets. However, along the jet centreline and within the interaction region $(x/d \geq 8)$, the structures in Jet A of the rect_min jet showed a 36% higher growth rate compared to those in Jet A for the round, square and rect_maj jets. Structures in Jet B grew along the jet centreline at comparable rates, irrespective of geometry while maintaining larger streamwise extent over structures in Jet A. Close to the free surface $(y_s/d = 0.5d)$, the structures are larger than those at the jet centreline but their streamwise growth is less than at the jet centreline.

- At the jet centreline, JPDF contours reveal that Reynolds shear stress producing events become increasingly important as the flow moves downstream into the merging region and are dominated by the fast u fluctuations. Within the shear layers, slow entrainment and fast ejection events dominate the contribution to Reynolds shear stress production.

5.1 Recommendations for Future Work

Some recommendation for future study on submerged three-dimensional twin jet flow are summarized below:

- In this study, planar PIV was used to obtain velocity measurements in the $x - y$ plane only and as such, details of the jets' dynamics in the spanwise direction were absent. To provide a better understanding of mixing and turbulence characteristics, it is recommended that a tomographic PIV be used to provide measurements of all three velocity components in a finite volume. Such measurements will facilitate analysis of complete Reynolds stress and velocity gradient tensors, as well as provide more insight into the dynamics of three-dimensional structures.
- Time-resolved PIV can be used to reveal temporal evolution of the flow and to characterize the time scales, two-point space-time correlations, and energy spectra.
- The measurement window of this study spanned $0 \leq x/d \leq 25$ which only captured the combined point of the rect_min geometry. For future studies, the examined flow field can be extended to further understand the jet dynamics in the combined region.

REFERENCES

Abdel-Rahman, A. A., Al-Fahed, S. F., & Chakroun, W. (1996). The near-field characteristics of circular jets at low Reynolds numbers. Mechanics Research Communications, 23(3), 313–324. https://doi.org/10.1016/0093-6413(96)00028-6

Adrian, R. J., Christensen, K. T., & Liu, Z. C. (2000). Analysis and interpretation of instantaneous turbulent velocity fields. Experiments in Fluids, 29(3), 275–290. https://doi.org/10.1007/s003489900087

Agelin-chaab, M. (2010). Experimental study of three-dimensional offset jets and wall jets. University of Manitoba, Winnipeg. Ph.D. Thesis

Agrawal, A., & Prasad, A. (2002). Properties of vortices in the self-similar turbulent jet. Experiments in Fluids, 33, 565–577. https://doi.org/10.1007/s00348-002-0507-7

Aleyasin, S. S., & Tachie, M. F. (2019). Statistical properties and structural analysis of three-dimensional twin round jets due to variation in Reynolds number. International Journal of Heat and Fluid Flow, 76, 215–230. https://doi.org/10.1016/j.ijheatfluidflow.2018.12.001

Aleyasin, S. S., Tachie, M. F., & Koupriyanov, M. (2017a). PIV measurements in the near and intermediate field regions of jets issuing from eight different nozzle geometries. Flow, Turbulence and Combustion, 99(2), 329–351. https://doi.org/10.1007/s10494-017-9820-3

Aleyasin, S. S., Tachie, M. F., & Koupriyanov, M. (2017b). Statistical properties of round , square and elliptic jets at low and moderate Reynolds numbers. ASME Journal of Engineering, 1–41. https://doi.org/10.1115/1.4036824

Anthony, D. G., & Willmarth, W. W. (1992). Turbulence measurements in a round jet beneath a free-surface. Journal of Fluid Mechanics, 243, 699–720.

Antonia, R. A., & Zhao, Q. (2001). Effect of initial conditions on a circuit jet. Experiments in Fluids, 31(3), 319–323. https://doi.org/10.1007/s003480100289

Ashcroft, G., & Zhang, X. (2005). Vortical structures over rectangular cavities at low speed. Physics of Fluids, 17(1). https://doi.org/10.1063/1.1833412

Ball, C. G., Fellouah, H., & Pollard, A. (2012). The flow field in turbulent round free jets. Progress in Aerospace Sciences, 50, 1–26. https://doi.org/10.1016/j.paerosci.2011.10.002

Brown, G. L., & Roshko, A. (1974). On density effects and large structure in turbulent mixing layers. Journal of Fluid Mechanics, 64(4), 775–816.

Christensen, K. T., & Wu, Y. (2005). Characteristics of vortex organization in the outer layer of wall turbulence. 4th International Symposium on Turbulence and Shear Flow Phenomena, 3, 1025–1030.

Coleman, H. W., & Steele, W. G. (1995). Engineering application of experimental uncertainty analysis. AIAA Journal, 33(10), 1888–1896. https://doi.org/http://dx.doi.org/10.2514/3.12742

Deo, R., Mi, J., & Nathan, G. (2007). Experimental investigations of the effect of Reynolds number on a plane jet. Proceedings of the 16th Australasian Fluid Mechanics Conference, 262–265.

Durve, A., Patwardhan, A. W., Banarjee, I., Padmakumar, G., & Vaidyanathan, G. (2012). Numerical investigation of mixing in parallel jets. Nuclear Engineering and Design, 242, 78–90. https://doi.org/10.1016/j.nucengdes.2011.10.051

Ead, S. A., & Rajaratnam, N. (2001). Plane turbulent surface jets in shallow tailwater. Journal of Fluids Engineering, 123(1), 121. https://doi.org/10.1115/1.1331556

El Hassan, M., & Meslem, A. (2010). Time-resolved stereoscopic particle image velocimetry investigation of the entrainment in the near field of circular daisy-shaped orifice jets. Physics of Fluids, 22(3), 7–26. https://doi.org/10.1063/1.3358465

Essel, Ebenezer E., & Tachie, M. F. (2017). Flow characteristics of submerged twin jets interacting with free surface. AIAA Journal, 55(10), 3622–3625. https://doi.org/10.2514/1.J055924

Essel, Ebenezer Ekow, Nematollahi, A., Thacher, E. W., & Tachie, M. F. (2015). Effects of upstream roughness and Reynolds number on separated and reattached turbulent flow. Journal of Turbulence, 16(9), 872–899. https://doi.org/10.1080/14685248.2015.1033060

Essel, Ebenezer Ekow, & Tachie, M. F. (2015). Roughness effects on turbulent flow downstream of a backward facing step. Flow, Turbulence and Combustion, 94(1), 125–153. https://doi.org/10.1007/s10494-014-9549-1

Essel, Ebenezer Ekow, & Tachie, M. F. (2018). Submerged turbulent twin jets interacting with a free surface and a solid wall. International Journal of Heat and Fluid Flow, 71, 27–38. https://doi.org/10.1016/j.ijheatfluidflow.2018.03.004

Evans, J. T. (1955). Pneumatic and similar breakwaters. Proceedings of Royal Society of London, 231(1187), 457–466. https://doi.org/10.1680/ipeds.1956.11769

Fellouah, H., Ball, C. G., & Pollard, A. (2009). Reynolds number effects within the development region of a turbulent round free jet. International Journal of Heat and Mass Transfer, 52(17–18), 3943–3954. https://doi.org/10.1016/j.ijheatmasstransfer.2009.03.029

Forliti, D. J., Strykowski, P. J., & Debatin, K. (2000). Bias and precision errors of digital particle image velocimetry. Experiments in Fluids, 28(5), 436–447. https://doi.org/10.1007/s003480050403

Ghahremanian, S., Svensson, K., Tummers, M. J., & Moshfegh, B. (2014). Near-field development of a row of round jets at low Reynolds numbers. Experiments in Fluids, 55(8). https://doi.org/10.1007/s00348-014-1789-2

Ghasemi, A., Roussinova, V., Balachandar, R., & Barron, R. M. (2015). Reynolds number effects in the near-field of a turbulent square jet. Experimental Thermal and Fluid Science, 61(C), 249–258. https://doi.org/10.1016/j.expthermflusci.2014.10.025

Grinstein, F. F., Gutmark, E., & Parr, T. (1995). Near field dynamics of subsonic free square jets. A computational and experimental study. Physics of Fluids, 7(6), 1483–1497. https://doi.org/10.1063/1.868534

Harima, T., Fujita, S., & Osaka, H. (2005). Turbulent properties of twin circular free jets with various nozzle spacing. Engineering Turbulence Modelling and Experiments 6, (1989), 501–510. https://doi.org/10.1016/B978-008044544-1/50048-0

Harima, T., Fujita, S., & Osaka, H. (2001). Mixing and diffusion processes of twin circular free jets with various nozzle spacing. 5th World Conference on Experimental Heat Transfer, Fluid Mechanics, and Thermodynamics, 2, 1017–1022. https://doi.org/10.1016/b978-0-444-81619-1.50022-8

Hashiehbaf, A., & Romano, G. P. (2013). Particle image velocimetry investigation on mixing enhancement of non-circular sharp edge nozzles. International Journal of Heat and Fluid Flow, 44, 208–221. https://doi.org/10.1016/j.ijheatfluidflow.2013.05.017

Ho, C., & Gutmark, E. (1987). Vortex induction and mass entrainment in a small-aspect-ratio elliptic jet. Journal of Fluid Mechanics, 179, 383-405

Hussain, A. K. M. F. (1983). Coherent structures—reality and myth. Physics of Fluids, 26(10), 2816. https://doi.org/10.1063/1.864048

Hussain, F., & Husain, H. S. (1989). Elliptic jets. Part 1. Characteristics of unexcited and excited jets. Journal of Fluid Mechanics, 208(1), 257. https://doi.org/10.1017/s0022112089002843

Hussein, H. J., Capp, S. P., & George, W. K. (1994). Velocity measurements in a high-Reynolds-number, momentum-conserving, axisymmetric, turbulent jet. Journal of Fluid Mechanics, 258, 31–75. https://doi.org/10.1017/S002211209400323X

Hutchins, N., Hambleton, W. T., & Marusic, I. (2005). Inclined cross-stream stereo particle image velocimetry measurements in turbulent boundary layers. Journal of Fluid Mechanics, 541, 21–54. https://doi.org/10.1017/S0022112005005872

Keane, R. D., & Adrian, R. J. (1990). Optimization of particle image velocimeters. Part I : Double pulsed systems. Measurement Science and Technology Optimization, 1, 1202–1215.

Ko, N. W. M., & Lau, K. K. (1989). Flow structures in initial region of two interacting parallel plane jets. Experimental Thermal and Fluid Science, 2(4), 431–449. https://doi.org/10.1016/0894-1777(89)90006-X

Laban, A., Aleyasin, S. S., Tachie, M. F., & Koupriyanov, M. (2019). Experimental investigation of nozzle spacing effects on characteristics of round twin free jets. Journal of Fluids Engineering, 141(7), 071201. https://doi.org/10.1115/1.4041989

Lee, S. J., & Baek, S. J. (1994). The effect of aspect ratio on the near-field turbulent structure of elliptic jets. Flow Measurement and Instrumentation, 5(3), 170–180. https://doi.org/10.1016/0955-5986(94)90016-7

Liepmann, D., & Gharib, M. (1992). The role of streamwise vorticty in the near field entrainement of round jets. Journal of Fluid Mechanics, 245, 642–668.

Lin, Y. E., & Sheu, M. J. (1990). Investigation of two plane paralleltunven ilated jets. Experiments in Fluids, 10, 17–22.

Madnia, C. K., & Bernal, L. P. (1994). Interaction of a turbulent round jet with the free-surface. Journal of Fluid Mechanics, 261, 305–332.

Mei, R., Adrian, R. J., & Hanratty, T. J. (1991). Particle dispersion in isotropic turbulence under Stokes drag and Basset force with gravitational settling. Journal of Fluid Mechanics, 225(4), 481–495. https://doi.org/10.1017/S0022112091002136

Meslem, A., Nastase, I., & Allard, F. (2010). Passive mixing control for innovative air diffusion terminal devices for buildings. Building and Environment, 45(12), 2679–2688. https://doi.org/10.1016/j.buildenv.2010.05.028

Mi, J., & Nathan, G. J. (2010). Statistical properties of turbulent free jets issuing from nine differently-shaped nozzles. Flow, Turbulence and Combustion, 84(4), 583–606. https://doi.org/10.1007/s10494-009-9240-0

Mi, J., Nathan, G. J., & Nobes, D. S. (2001). Influence of jet exit conditions on the passive scalar field of an axisymmetric free jet. Journal of Fluids Engineering, 123(4), 878. https://doi.org/10.1115/1.1412460

Mi, J., Xu, M., & Zhou, T. (2013). Reynolds number influence on statistical behaviors of turbulence in a circular free jet. Physics of Fluids, 25(7). https://doi.org/10.1063/1.4811403

Miller, D. R., & Comings, E. W. (1960). Force-momentum fields in a dual-jet flow. Journal of Fluid Mechanics, 7(2), 237–256. https://doi.org/10.1017/s0022112060001468

Namer, I., & Ötügen, M. V. (1988). Velocity measurements in a plane turbulent air jet at moderate Reynolds numbers. Experiments in Fluids, 6(6), 387–399. https://doi.org/10.1007/BF00196484

Nematollahi, A., & Tachie, M. F. (2018). Time-resolved PIV measurement of influence of upstream roughness on separated and reattached turbulent flows over a forward-facing step. AIP Advances, 8(10). https://doi.org/10.1063/1.5063455

Okamoto, T., Yagita, M., Watanabe, A., & Kawamura, K. (1985). Interaction of twin turbulent ciruclar jet. Jsme, 28(238), 617–622. https://doi.org/10.1248/cpb.37.3229

Prasad, A. K., Adrian, R. J., Landreth, C. C., & Offutt, P. W. (1992). Effect of resolution on the speed and accuracy of particle image velocimetry interrogation. Experiments in Fluids, 13(2–3), 105–116. https://doi.org/10.1007/BF00218156

Quinn, W. R. (1992). Turbulent free jet flows issuing from sharp-edged rectangular slots : the influence of slot aspect ratio. Experimental Thermal and Fluid Science, 5, 203–215.

Quinn, W. R. (2006). Upstream nozzle shaping effects on near field flow in round turbulent free jets. European Journal of Mechanics, B/Fluids, 25(3), 279–301. https://doi.org/10.1016/j.euromechflu.2005.10.002

Raffel, M., Willert, C. E., Wereley, S. T., & Kompenhans, J. (2007). Particle image velocimetry. Springer. https://doi.org/10.1007/978-3-540-72308-0

Rahman, Mohammad S., & Tachie, M. F. (2018). Reynolds number effect on flow characteristics of surface single and twin jets. Journal of Hydraulic Research, 1686. https://doi.org/10.1080/00221686.2018.1522380

Rahman, Mohammad Shajid. (2019). Experimental study on turbulent characteristics of surface attaching jets. University of Manitoba, Winnipeg. Ph.D. Thesis

Rahman, Mohammad Shajid, Tay, G. F. K., Essel, E. E., & Tachie, M. F. (2018). Effects of offset height on the turbulent characteristics of a surface attaching jet. International Journal of Heat and Fluid Flow, 71, 305–321. https://doi.org/10.1016/j.ijheatfluidflow.2018.04.012

Rahman, Mohammad Shajid, Tay, G. F. K., & Tachie, M. F. (2019). Effects of nozzle geometry on turbulent characteristics and structure of surface attaching jets. Flow, Turbulence and Combustion. https://doi.org/10.1007/s10494-019-00047-7

Raiford, J. P., & Khan, A. A. (2009). Investigation of circular jets in shallow water. Journal of Hydraulic Research, 47(5), 611–618. https://doi.org/10.3826/jhr.2009.3474

Rajaratnam, N., & Humphries, J. A. (1984). Turbulent non-buoyant surface jets. Journal of Hydraulic Research, Vol. 22, pp. 103–115. https://doi.org/10.1080/00221688409499387

Ricou, F. P., & Spalding, D. B. (1961). Measurements of entrainment by axisymmetrical turbulent jets. Journal of Fluid Mechanics, 11, 21–32.

Robinson, S. (1991). Coherent motions in the turbulent boundary layer. Annual Review of Fluid Mechanics, 23(1), 601–639. https://doi.org/10.1146/annurev.fluid.23.1.601

Sankar, G., Balachandar, R., & Carriveau, R. (2008). Tailwater effects on the characteristics of a square jet near a free-surface. Journal of Hydraulic Research, 46(4), 504–515. https://doi.org/10.3826/jhr.2008.3043

Schadow, K. C., Gutmark, E., Parr, D. M., & Wilson, K. J. (1988). Selective control of flow coherence in triangular jets. Experiments in Fluids, 6(2), 129–135. https://doi.org/10.1007/BF00196464

Shinneeb, A. M., Balachandar, R., Bugg, J. D. (2011). Confinement effects in shallow-water jets. Journal of Hydraulic Engineering, 137(3), 300–314. https://doi.org/10.1061/(ASCE)HY.1943-7900.0000306

Shinneeb, A.-M., Bugg, J. D., & Balachandar, R. (2011). Coherent structures in shallow water jets. Journal of Fluids Engineering, 133(1), 011203. https://doi.org/10.1115/1.4003194

Swean, T. F., Ramberg, S. E., Plesniak, M. W., & Stewart, M. B. (1989). Turbulent surface jet in channel of limited depth. Journal of Hydraulic Engineering, 115(12), 1587–1606. https://doi.org/10.1061/(ASCE)0733-9429(1989)115:12(1587)

Tanaka, E. (1970). The interference of two-dimensional parallel jets (1st report, experiments on dual jet). Transactions of the Japan Society of Mechanical Engineers, 13(56), 272–280. https://doi.org/10.1299/kikai1938.35.1257

Tanaka, E. (1974). The interference of two-dimensional parallel jets (2nd report, experiments on the combined flow of dual jet). The Japan Society of Mechanical Engineers, 17(109), 920–

927. https://doi.org/10.1299/jsme1958.17.920

Tay, G. F. K. (2015). Experimental Study of Particle-Induced Turbulence Modification in the Presence of a Rough Wall. University of Manitoba, Winnipeg. Ph.D. Thesis

Tay, G. F. K., Mishra, A., Kuhn, D. C. S., & Tachie, M. F. (2017). Free surface effects on the statistical properties of a submerged rectangular jet. Physics of Fluids, 29(2). https://doi.org/10.1063/1.4975155

Tay, G. F. K., Rahman, M. S., & Tachie, M. F. (2017a). Characteristics of a horizontal square jet interacting with the free surface. Physical Review Fluids, 2(6). https://doi.org/10.1103/PhysRevFluids.2.064607

Tay, G. F. K., Rahman, M. S., & Tachie, M. F. (2017b). Characteristics of a square jet interacting with the free surface. Physical Review Fluids.

Tropea, C., Yarin, A. L., & Foss. J. F. (2007). Handbook of experimental fluid mechanics. Springer. https://doi.org/10.1017/CBO9781107415324.004

Tsunoda, H., Shimizu, Y., & Kashiwagi, T. (2006). Plane offset jet discharged into water of finite depth. JSME International Journal Series B, 49(4), 1111–1117. https://doi.org/10.1299/jsmeb.49.1111

Volino, R. J., Schultz, M. P., & Flack, K. a. (2007). Turbulence structure in rough- and smooth-wall boundary layers. Journal of Fluid Mechanics, 592, 263–293. https://doi.org/10.1017/S0022112007008518

Vouros, A., & Panidis, T. (2008). Influence of a secondary, parallel, low Reynolds number, round jet on a turbulent axisymmetric jet. Experimental Thermal and Fluid Science, 32(8), 1455–1467. https://doi.org/10.1016/j.expthermflusci.2008.03.007

Walker, D. T., Chen, C.-Y., & Willmarth, W. W. (1995). Turbulent structure in free-surface jet flows. Journal of Fluid Mechanics, 291, 223–261. https://doi.org/10.1017/S0022112095002680

Wallace, J. M., & Brodkey, R. S. (1977). Reynolds stress and joint probability density distributions in the u-v plane of a turbulent channel flow. Physics of Fluids, 20(3), 351–355. https://doi.org/10.1063/1.861897

Wen, Q., Dong Kim, H., Zheng Liu, Y., & Chun Kim, K. (2014). Structure analysis of a low reynolds number turbulent submerged jet interacting with a free surface. Journal of Fluids Engineering, 136(10), 101104. https://doi.org/10.1115/1.4027620

Wen, Q., Kim, H. D., Liu, Y. Z., & Kim, K. C. (2014). Dynamic structures of a submerged jet interacting with a free surface. Experimental Thermal and Fluid Science, 57, 396–406. https://doi.org/10.1016/j.expthermflusci.2014.06.005

White, B. L., & Nepf, H. M. (2007). Shear instability and coherent structures in shallow flow adjacent to a porous layer. Journal of Fluid Mechanics, 593, 1–32. https://doi.org/10.1017/S0022112007008415

Wygnanski, I., & Fiedler, H. (1969). Some measurements in the self preserving jet. Journal of Fluid Mechanics, 38(3), 577–612.

Xu, G., & Antonia, R. A. (2002). Effect of different initial conditions on a turbulent round free jet. Experiments in Fluids, 33(5), 677–683. https://doi.org/10.1007/s00348-002-0523-7

Xu, M., Pollard, A., Mi, J., Secretain, F., & Sadeghi, H. (2013). Effects of Reynolds number on some properties of a turbulent jet from a long square pipe. Physics of Fluids, 25(3). https://doi.org/10.1063/1.4797456

Zang, B., & New, T. H. (2015). On the wake-like vortical arrangement and behaviour associated with twin jets in close proximity. Experimental Thermal and Fluid Science, 69, 127–140. https://doi.org/10.1016/j.expthermflusci.2015.08.004